Kinematic Subduction Rate Of Labrador Sea Water From an Eddy-Permitting Numerical Model

Peggy Courtois[1] [iD]**, Yarisbel Garcia-Quintana[1]** [iD]**, Xianmin Hu[1,2]** [iD]**, and Paul G. Myers[1]** [iD]

[1]Department of Earth and Atmospheric Sciences, University of Alberta, Edmonton, Alberta, Canada, [2]Bedford Institute of Oceanography, Dartmouth, Nova Scotia, Canada

Abstract We use an eddy-permitting, 1/12° regional configuration of the Nucleus for European Modelling of the Ocean (NEMO) model to examine water mass subduction rates in the Labrador Sea for the 2002–2013 period. An instantaneous kinematic subduction approach is implemented to calculate the subduction rate of Labrador Sea Water (LSW). By following the outcrop positions of a given isopycnal range, we calculate the vertical transport of a water mass from the mixed layer into the permanent thermocline over the course of a year. We examine the importance of the various terms in this approach, including the evolution of the Mixed Layer Depth (MLD), the advection across the base of the Mixed Layer (ML), and the vertical velocity at the base of the ML. We find that the subduction rate is not greatly affected by the definition of the MLD, as long as the integration time is long enough for the subduction-obduction processes to balance each other. The total LSW subduction rate is ~4–5 Sv, with similar rates for both Upper (ULSW) and Classical LSWs (CLSW), (~2–2.5 Sv). After 2008, a shift in the LSW density is found in the simulation. CLSW reaches a maximum rate of 6 Sv in 2008, which is mainly inferred by the instantaneous ML change.

1. Introduction

Part of the North Atlantic Ocean, the Labrador Sea (LS), is situated between Greenland, the Canadian Arctic Archipelago (CAA) and eastern Canada (cf. Figure 1). Three main currents bound the LS (Cuny et al., 2002): the West Greenland Current (WGC) providing fresh and cold water from the Nordic Seas, the Baffin Island Current (BIC) bringing cold water from the Arctic Ocean (Münchow et al., 2015), and the Labrador Current (LC) carrying fresh and cold water from Baffin Bay above the East Canadian shelf (Lazier & Wright, 1993). Further offshore the West Greenland shelf, at intermediate depth, the WGC brings warm and saline Irminger water into the LS (Fratantoni & Pickart, 2007; Gascard & Clarke, 1983; Grist et al., 2014). The LS is one of the few places where deep convection takes place, allowing gas and heat exchanges between the atmosphere and the deep ocean. This process is characterised by strong winds cooling the ocean surface, producing major heat losses (exceeding 400 W/m^2 in cold months; e.g., Moore et al., 2014; Schulze et al., 2016), especially at the beginning of winter (Marshall & Schott, 1999). This atmospheric forcing disturbs the already weakly stratified water column, producing a uniformly denser water mass, which finally spreads along the deepest isopycnals (Clarke & Gascard, 1983). The resulting water mass is called Labrador Sea Water (LSW) and is one of the few water masses created by deep convection. The LSW is characterized by a minimum in salinity and potential vorticity and a maximum in chlorofluorocarbon (CFC) and oxygen concentrations (Clarke & Gascard, 1983).

Three major pathways are known for the LSW (Rhein et al., 2002). A part of the LSW spreads to the Northeast directly from the convection site into the Irminger Sea. Another part of the LSW joins the LC, flowing south along the continental shelf and around Grand Banks into the subtropics to join the Deep Western Boundary Current (DWBC). As the LC splits near Flemish Cap, some LSW is entrained into the North Atlantic Current (NAC), which, in turn, splits to flow eastward crossing the mid-Atlantic ridge (Biló & Johns, 2019) and to finally mix with the warm and saline Mediterranean Water (MW). The remaining NAC flows to the north into the Irminger Sea and then to the LS via the Irminger Current (IC; see Figure 1). By combining Lagrangian and Eulerian observations, a recent study showed additional interior, equatorward pathways to export the LSW to the subtropics (Gary et al., 2012). The dispersion of the LSW in the North Atlantic contributes to the lower limb of the Meridional Overturning Circulation (MOC) and consequently participates in the ventilation of the deep layers of the world ocean. Many observational
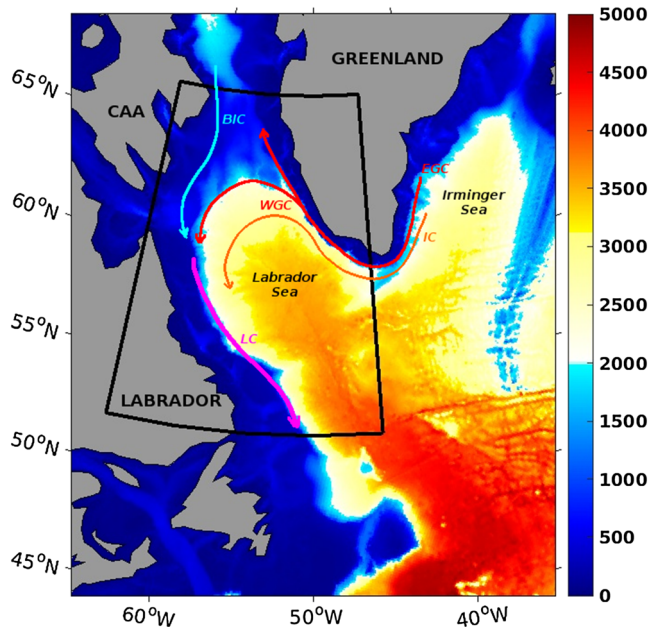
Figure 1. Map showing a part of the subpolar gyre in the North Atlantic Ocean, focussing on the Labrador Sea with the associated currents (WGC, BIC, IC, and LC, as defined in the text). The studied area is represented by the black rectangle. The color scale shows the depth in meters.

(Lozier, 2012; Li & Lozier, 2018) and numerical (Böning et al., 2006; Marsh et al., 2005; Pickart et al., 2003) studies have shown a link between the LSW formation rate and the strength of the MOC. However, quantifying the impact of the LSW on the MOC is still under debate (Mauritzen & Häkkinen, 1999; Pickart & Spall, 2007). Yashayaev and Loder (2017) recently showed that deep convection in the LS has intensified since 2012, producing the most voluminous water mass since 1994, while Parker and Ollier (2016) argued there is no clear evidence of increasing nor decreasing strength of the AMOC. Quantifying the subpolar AMOC and its variability is one of the goals of the Overturning in the Subpolar North Atlantic Program (OSNAP), as well as studying its connectivity to the deep boundary current system (Lozier et al., 2017).

LSW has been the center of interest for many decades (Sverdrup et al., 1942; Worthington, 1976; Straneo, 2006; Kieke & Yashayaev, 2015) and is still an active research area in terms of its formation (Speer & Tziperman, 1992; Yashayaev, 2007; Yashayaev & Loder, 2016), circulation (Haine et al., 2008; Rhein et al., 2015; Talley & McCartney, 1982), and variability (Dickson et al., 1996; Kieke & Yashayaev, 2015; van Aken et al., 2011). One of the difficulties in studying LSW is to define the water mass properties. In their paper, Talley and McCartney (1982) defined the LSW with a temperature of 3.3–3.4°C and a salinity of 34.86–34.88 gkg^{-1}. Pickart et al. (1996) first mentioned Upper Labrador Sea Water (ULSW) in comparison to the Classical Labrador Sea Water (CLSW). Both water classes are generated by convection, but their production depends on external factors, like atmospheric forcing, location, and the year. ULSW is slightly warmer and fresher than CLSW and therefore slightly shallower (Kieke et al., 2006). A different approach is now used to define LSW, based on water masses produced over a specific period of time (Haine et al., 2008; Yashayaev, 2007; Yashayaev et al., 2007; Yashayaev & Loder, 2016). This approach allows to consider the slight variations between the produced water masses in terms of properties and depths. For example, Yashayaev (2007) described two LSW classes, $LSW_{1987-1994}$ and LSW_{2000}, which reflect the LSW production over a period of time ($LSW_{1987-1994}$) or a specific year (LSW_{2000}). Recently, a new LSW class was produced during the winters of 2014 and 2015, $LSW_{2014-2015}$, reaching a maximum depth of 1,700 m, the deepest since 1994 (Yashayaev & Loder, 2016).

Variability in the production of LSW is mainly due to the atmospheric forcing, which plays a role in the intensity of the convection (Schulze et al., 2016; Yashayaev & Clarke, 2006). The North Atlantic Oscillation (NAO) represents the major mode of atmospheric variability. Its index, the NAO index, is based on the anomalies of sea level pressure gradient, from which anomalous winds are inferred (Hurrel, 1995). During high NAO index (strong westerlies) years, the center of the LS is expected to experience enhanced heat loss, leading to more vigourous and deeper convection. Several studies have shown that convection was weaker during years with low NAO index (Dickson et al., 1996; Lazier, 1980). Additionally, the extreme negative phase of the NAO tends to generate a significant perturbation of the surface salinity field, caused by major freshwater input from the Arctic into the Labrador Basin via the WGC, and/or Baffin Bay (Belkin et al., 1998; Dickson et al., 1988). These exceptional freshwater anomalies (e.g., the Great Salinity Anomalies [GSA] in the 1970s identified by Dickson et al., 1988) tend to insulate the deep ocean from the atmosphere, increasing surface buoyancy while reducing the oceanic heat loss (Gelderloos et al., 2012). Given the ongoing changes in high-latitude freshwater sources (e.g., Haine et al., 2015), recent work has focused on the potential impact on LSW formation from a release of the freshwater stored in the Beaufort Gyre (e.g., Stewart & Haine, 2013) or the rapidly increased discharge from the Greenland Ice Sheet (e.g., Bamber et al., 2018). Multiple studies indicate that if the freshwater input from Greenland is large enough, LSW formation will be significantly impacted (e.g., Böning et al., 2016; Yang et al., 2016).

Estimates of LSW formation rate differ greatly from one study to another, from 2 Sv (i.e., 1 Sv =10^6m^{3}s^{-1}) (Worthington, 1976) up to 12.7 Sv (Marshall & Schott, 1999) during an active winter. This difference is

Table 1

Nonexhaustive Table Summarizing the Various Estimates of LSW Formation Rate, Depending on the Method Considered (Hydrographic Data-Based Method, CFC Inventories, Air Sea flux, and Numerical Studies)

Hydrographic data-based approach			
3.9 Sv	LSW	1976	Clarke and Gascard (1983)
4.4–5.6 Sv	LSW	1988–1997	Rhein et al. (2002)
2 Sv	LSW	1990–1997	Pickart and Spall (2007)
CFC inventories			
2.2 Sv	ULSW	1970–1990	Smethie and Fine (2001)
7.4 Sv	CLSW	1970–1990	Smethie and Fine (2001)
3.2–3.3 Sv	ULSW	1970–1997	Kieke et al. (2006)
Air sea flux			
3.4 Sv	LSW	1980–1997	Marsh (2000)
2.1–3.9 Sv	LSW	1960–1999	Myers and Donnelly (2008)
Numerical Studies			
8.6 Sv	LSW	—	McCartney and Talley (1984)
8–9 Sv	LSW	1980–1986	Mauritzen and Häkkinen (1999)
7 Sv	LSW	1985–2002	Marsh et al. (2005)

mainly due to the method considered, the definition of the LSW, and the formation rate, as well as the period studied. Table 1 shows a nonexhaustive list of various estimates of the LSW rate, depending on the method used. Hydrographic data-based approaches, for example, yield a total water mass transformation of 2 Sv for the years 1990–1997 using repeated cross sections of the World Ocean Circulation Experiment (WOCE) (Pickart & Spall, 2007). Based on CFC inventories, Smethie and Fine (2001) found 2.2 Sv for ULSW and 7.4 Sv for CLSW for the 1970–1990 time period. As the deep convection is driven by buoyancy, air sea flux-related methods are commonly used to determine the water mass formation in the North Atlantic Ocean (Khatiwala et al., 2002; Marsh, 2000; Speer et al., 1995; Wright, 1972). Marsh (2000) obtained a time series of the production rate of intermediate water (LSW) using a global air-sea heat and freshwater flux climatology. The author found a mean of 3.4 Sv for the 1980–1997 time period, with a maximum rate of 10 Sv in 1990 with a high NAO index. Based on surface hydrographic fields and NCEP-NCAR reanalysis fluxes, Myers and Donnelly (2008) found a mean long-term transformation of 2.1 ± 0.2 to 3.9 ± 0.3 Sv. One discrepancy with air sea fluxes based methods is that physical processes, for example, the mixed layer (ML) processes, are not represented and lack of ocean surface data may lead to underestimated rates. From a different view, numerical studies tend to take into account additional features, such as advection and mixing processes (Böning et al., 1996; Worthington, 1976). McCartney and Talley (1984) used a box model to estimate the conversion rate in the Northern North Atlantic Ocean. They estimated the production of LSW at 8.6 Sv, which is in agreement with the estimation of 8–9 Sv by Mauritzen and Häkkinen (1999). A major assumption made in determining the transformation rate of the LSW is to assume that the LSW from the previous years is totally distributed in the SPG. This is clearly not the case as deep convection acts on the previously formed LSW (Lazier et al., 2002; Yashayaev & Loder, 2016). This assumption leads to an overestimation of the annual transformation rate. Brandt et al. (2007) have investigated the transformation and export of the newly ventilated LSW and have found a transformation rate of 6.8 Sv.

A different approach calculating the subduction rate has been widely used to quantify the transfer of water from the ML to the stratified thermocline (Cushman-Roisin, 1987; Da Costa et al., 2005; Marshall et al., 1993; Williams, 2001). For example, Da Costa et al. (2005) used this approach to quantify the water mass subduction rates in the North Atlantic Ocean subtropical gyre in a high-resolution numerical model and found a total of 12.2 Sv for the subduction rate for the subtropical mode waters (26.2–26.6 kg m^{-3}). In this present work, we use an eddy-permitting, 1/12° regional configuration of the Nucleus for European Modelling of the Ocean (NEMO) model to examine water mass subduction rates in the LS. Similarly to Da Costa et al. (2005), we use an instantaneous kinematic subduction approach to calculate the vertical transport of a water mass from the ML into the permanent thermocline over the course of a year. This method has the advantage to consider the direct interaction of the ML and the interior of the ocean, by considering vertical and lateral exchanges through the ML base. Combined with model output, it allows to calculate the subduction rate over large areas. The disadvantage is that, like many others, this method accumulates the remaining LSW from previous years. Both method and model are described in section 2. In section 3.1, we examine the impact of the MLD, while the formation rates for ULSW and CLSW will be discussed in section 3.2. The various terms defined in the approach will be presented in section 3.3, and the concluding remarks in section 4.

2. Method and Data

2.1. Numerical Model

The NEMO numerical framework Version 3.4 (Madec, 2008) is used with the Arctic and Northern Hemisphere Atlantic (ANHA) configuration, with a 1/12° resolution (ANHA12). The ANHA12 configuration is a subdomain of the global ORCA12 mesh. It covers the Arctic and the North Atlantic Ocean down to 20° S, including the Mediterranean Sea. The model is a three-dimensional (3-D) numerical model coupling a primitive-equation ocean generation circulation model with a dynamic-thermodynamic sea ice model, the Louvain-la-Neuve sea ice model LIM2 (Fichefet & Maqueda, 1997), with an Elastic Viscous
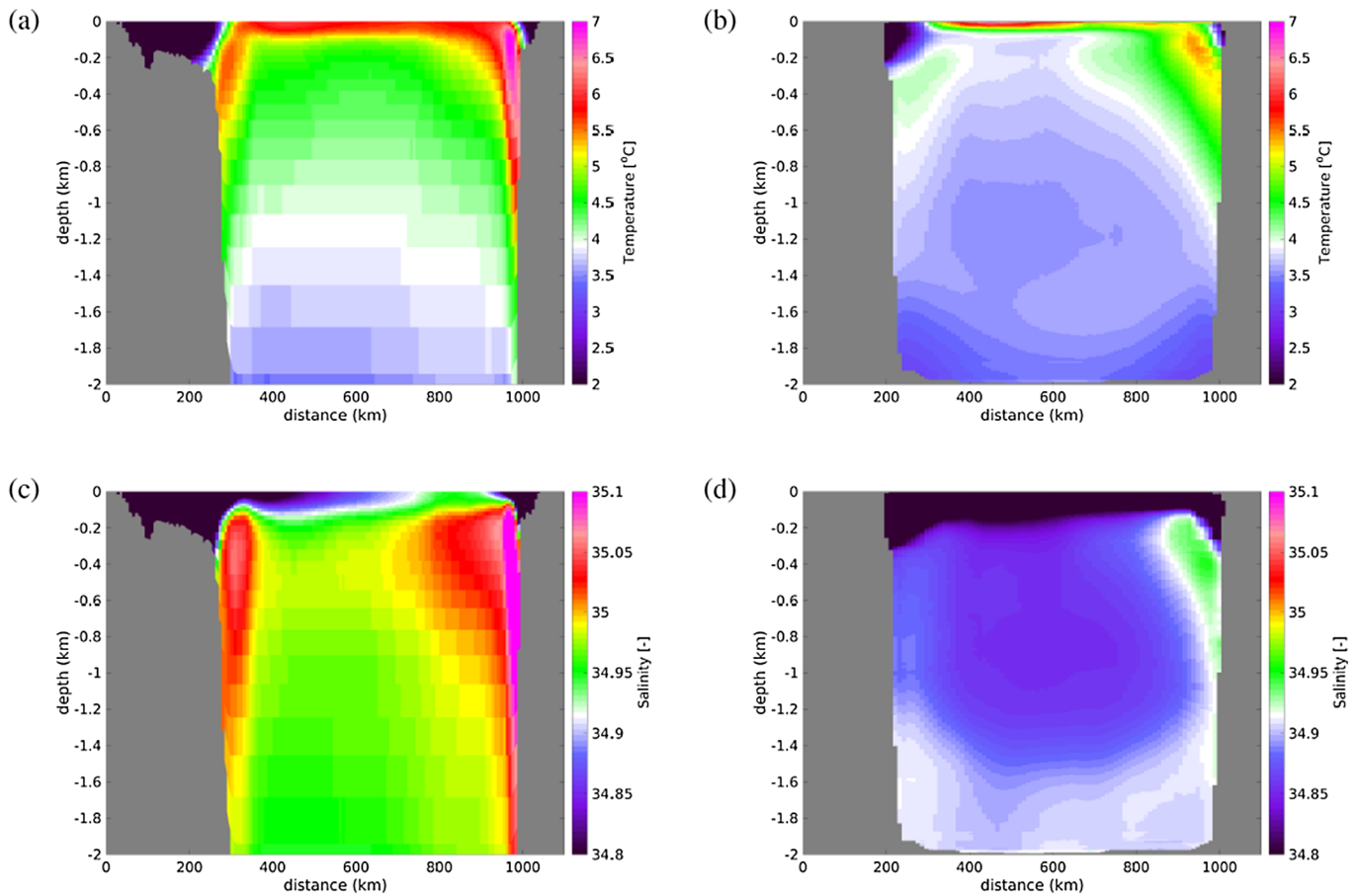
Figure 2. Comparison of the temperature (top) and salinity (bottom) along the AR7 Wsection, for both model fields (left) and Argo data (right) (2004–2016).

Plastic ice rheology (Hunke & Dukowicz, 1997). The experiment output used here was from January 2002 to December 2013, with 5-day output. The initial and open boundary conditions are taken from Global Ocean Reanalyses and Simulations (GLORYS) data set (Ferry et al., 2010), from GLORYS2v3. The hourly 33 km resolution atmospheric forcing comes from the Canadian meteorological centre Global deterministic prediction system ReForecast (CGRF Smith et al., 2014). Runoff is interannual monthly runoff, based on Dai and Trenberth Global River Flow and Continental Discharge Dataset (up to 2007) (Dai & Trenberth, 2002; Dai et al., 2009), including Greenland melt data up to 2010 from Bamber et al. (2012). We use repeating perpetual years to complete the missing years.

The ocean module contains the vertical mixing, parametrized by a Turbulent Kinetic Energy closure scheme. The vertical eddy viscosity and diffusivity are set to $1 \times 10^{-4}\,\mathrm{m^2 s^{-1}}$ and $1 \times 10^{-5}\,\mathrm{m^2 s^{-1}}$, respectively. There is no temperature and salinity restoring in this simulation, in order to let the model freely evolve through time and therefore to better understand its limitations. The vertical mesh is defined by 50 levels. The first 22 levels span the first 100 m, smoothly increasing from 1.05 m at the surface to 15.8 m thick for the 22nd level (92.3 m). The thickness of each level continues to increase gradually, to reach 458.39 m thick for the last level at 5,728 m. The horizontal resolution spans 1.9 km in Dease Strait (northern Canada) to 9.3 km at the equator, with a resolution around 5 km in the LS. The large eddies and rings shed from the WGC, typically with a radius of greater than 10 km (de Jong et al., 2014; Gelderloos et al., 2011; Lilly et al., 2003), can thus be generally resolved by the model.

2.2. Model Evaluation

The given model configuration ANHA12 has previously been used to study processes in the Canadian Arctic (e.g., Hughes et al., 2017, 2018), where mixing and sea ice were well represented, as well as volume and
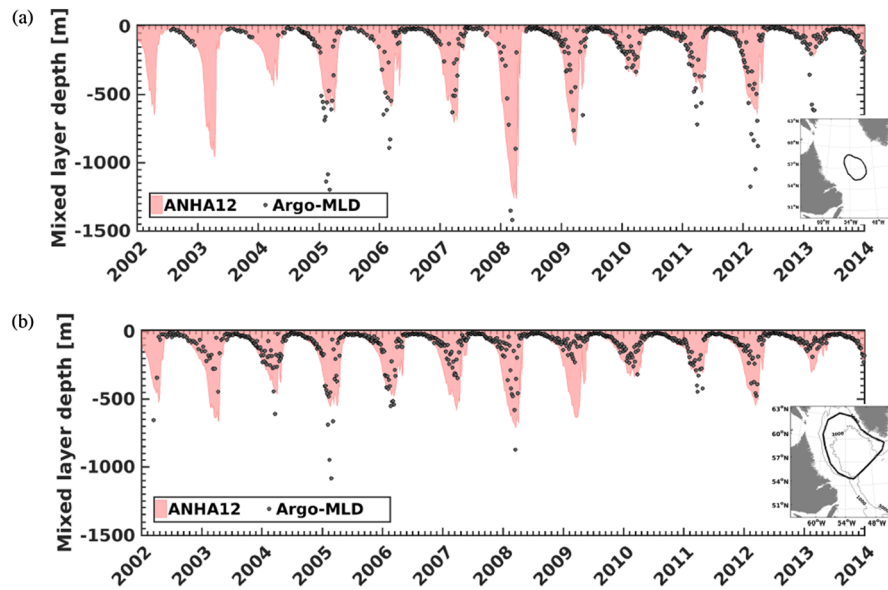
Figure 3. Comparison of the model MLDs (in pink) with the Argo mixed layer depths (black dots) in meters, within the interior of the Labrador Sea. Two areas are considered: a small region showing the interior Labrador Sea (top) and a larger one based on the 1,000 misobaths (bottom).

freshwater exports to the LS (Grivault et al., 2018). Pennelly et al. (2019) used the same experiment as ours to examine cross-shelf freshwater exchange into the interior of the LS. They compared model current speed with geostrophic current speed derived from AVISO data, averaged over 2002–2013 (Pennelly et al., 2019). The authors found a good correspondence with the fast boundary currents along the shelf break and a more quiescent interior. The simulation produces slightly faster boundary currents, although the satellite product has greater variability.

We compared temperature and salinity along the AR7W section, considering both model fields and Argo data (Figure 2). To plot temperature/salinity sections with Argo data, we selected profiles found in the Labrador Sea with a quality control (QC) flag on pressure, temperature, and salinity set to 1, 2, or 5 to 8, which are considered as good data. We used all Argo profiles available with these flags for the period January 2004 to December 2013. Temperature and salinity were then interpolated onto a regular depth axis going from the surface down to 2n000 m with a 5 m resolution. We, then, created a regular axis along the AR7W section with a 0.1° resolution to map the Argo data along this section. At each depth, grid point mapping was limited to a 0.5° radius disk containing at least 10 points. Argo data contained in this disk were averaged, and the value was assigned to the corresponding coordinate and depth along the AR7W section. Model fields were linearly interpolated from the model grid onto the same AR7W grid, also averaged over January 2004 to December 2013.

As the Argo floats are constrained to the deeper parts of the basin, the shelves are not clearly resolved in the observed figures. However, both the model and observations do represent cold and fresh boundary currents, with similar fronts at the shelf break. There is a greater penetration of surface heating in the model. Low-salinity water does not extend all the way across the section at the surface. This is a limitation in the model, which impacts the stratification and, hence, the strength of convection. Along the shelf break of the WGC, the warm and salty Irminger Water can be seen. It is too warm and salty in the model, as well as extending to a too great depth (up to 1,200 m, cf. 800 m with Argo data). This is a common issue in numerical models of this region (e.g., Rattan et al., 2010). The presence of excess Irminger Water in the model will translate into excess water flowing south offshore of the LC. This results in a model drift in the interior of the LS, leading to an excessively warm and salty basin. The resulting MLD is not as impacted as expected due to a temperature-salinity compensation providing reasonable MLD as explained in Courtois et al. (2017).

We next compared the model Mixed Layer Depths (MLDs) with ML depths estimated from Argo, within the interior of the LS (Figure 3). We defined two regions, a larger one based on the 1,000 m isobaths (and the AR7W section) and a smaller one, consistent with the interior LS mask used by Yashayaev and Loder
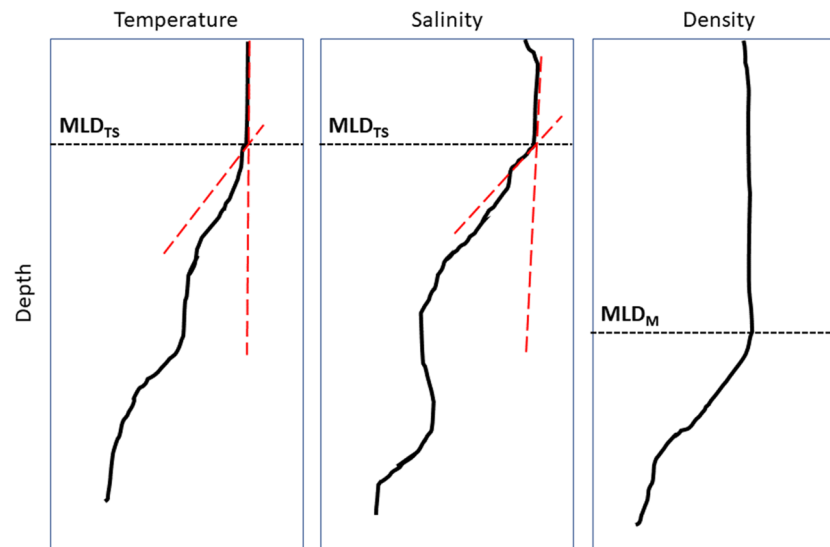
Figure 4. Schematic showing the MLD_{TS} obtained with our fitting method on temperature and salinity profiles (the fittings are shown in red). The MLD_M provided in the suite of outputs is based on a density criterion of 0.01 kg m^3. This situation is mainly seen during deep convection, when temperature and salinity compensate each other.

(2016). We thus compared the average model MLD (calculated via density criteria) within each mask with the MLD determined from all available Argo profiles within each masked region. The Argo MLD is computed using the scheme of Holte and Talley (2009). In general, the model effectively captures the interannual variability of the observed Argo-based MLDs. Despite the property drift highlighted above, the model does not necessarily overestimates the observed MLDs. However, the model does generally have a broader region of deep MLs than is understood from observations (consistent with many such modelling studies). Given the generally good correspondence between the model and the observations in terms of MLD, especially in terms of seasonal and interannual variability, we think the model is thus a reasonable tool to use for our study of kinematic subduction of LSW.

2.3. Mixed Layer Depth

The diagnostic MLD provided in the suite of model outputs is calculated using a traditional density difference criterion of 0.01 kg m^{-3}. In our previous work (Courtois et al., 2017), we have shown that this latter MLD was overestimated during strong deep convection events, due to temperature-salinity compensation. To overcome this discrepancy, we have developed an algorithm, originally based on observational data (Holte & Talley, 2009), which determines the MLD as the intersection of two fittings, one fitting on the ML and the other one on the layer underneath, on temperature and salinity profiles. If the MLD found is shallower than the diagnostic MLD provided by the model (MLD_M), then the new MLD (MLD_{TS}) is recorded. Figure 4 shows a schematic of temperature, salinity, and density profiles, where both MLDs are represented.

In Courtois et al. (2017), we compared the MLDs obtained with both methods, the traditional density difference criterion of 0.01 kg m^{-3} and our fitting method, both spatially and temporally. We found that MLDs obtained with our approach were more realistic than those obtained with traditional density difference, through the whole model experiment (2002–2011). We compared MLDs from both methods with observational MLDs from Argo data for the winter 2008. The maximum MLD with Argo float was around 1,680 m in winter 2008. The MLDs from the density-based method exceeds 2,500 m for the entire Labrador basin, with a maximum reaching the bottom topography. Our approach showed maximum MLDs around 2,200 m. Further details regarding the method and its validation can be found in Courtois et al. (2017). In the result section, the subduction rate of the LSW will be shown for both MLDs, one from the model output based on density criterion and the other from the fitting method. We chose to present both approaches, because of the important role of the MLD in deep convection, and to answer the question of the impact of an overestimated MLD in our calculations.
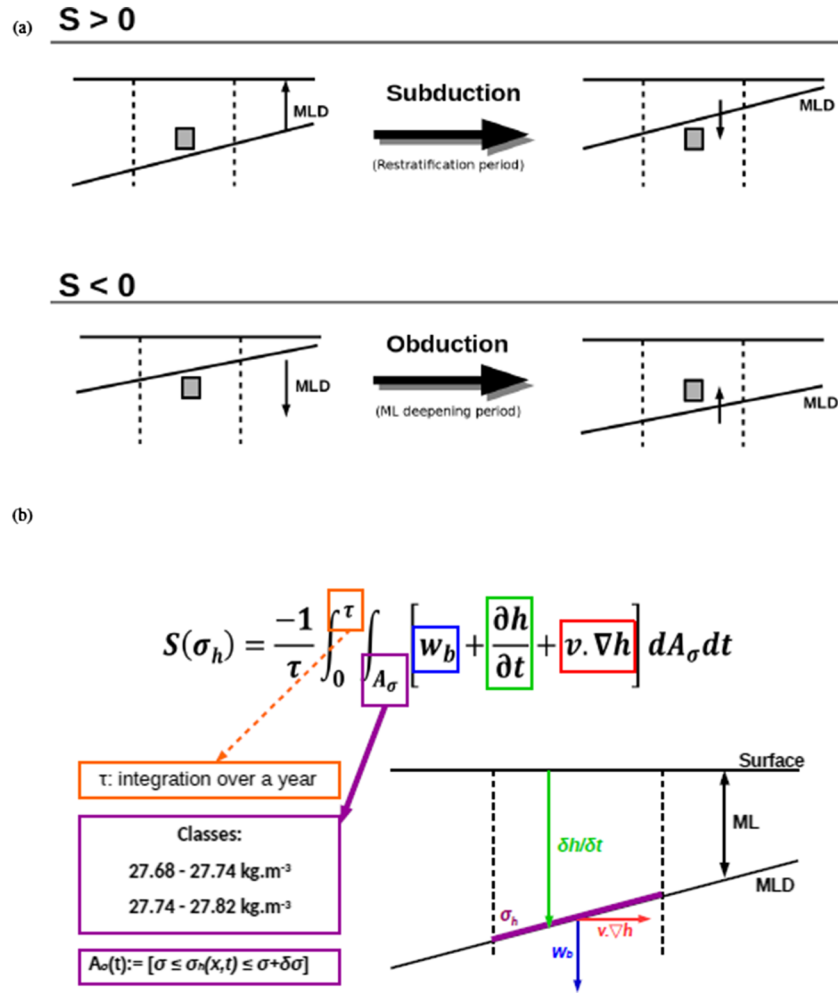
$$S(\sigma_h) = \frac{-1}{\tau} \int_0^\tau \int_{A_\sigma} \left[w_b + \frac{\partial h}{\partial t} + v.\nabla h \right] dA_\sigma dt$$

Figure 5. (a) Schematic showing the subduction ($S>0$, top) and the obduction ($S<0$, bottom) processes. In both cases, the gray cell is fixed. The base of the MLD is moving upward (downward) for the subduction (obduction) process. The large horizontal black arrows correspond to a short amount of time for both processes to occur. During that time, the gray cell (fixed) crosses the moving base of the MLD in the opposite direction (downward [upward] arrow on the right-hand side for the subduction [obduction] process). (b) Schematic representing the mixed layer with all the associated terms from Equation 3. The formal definition of suduction applies to fluid that "escapes" the mixed layer to reach the permanent pycnocline. Under a repeating seasonal cycle, a subducting parcel needs to move laterally or vertically (deeper) to a location where the winter mixed layer depth deepens to a lesser extent in the following winter. The instantaneous ML $\left(\frac{\partial h}{\partial t} \right)$ is shown in green, the advective terms ($v \cdot \nabla h$) that represent fluid crossing the laterally sloping ML base are shown in red, and the term based on the vertical velocity (w_b) is shown in blue. The instantaneous mixed layer density (σ_h) is in purple and corresponds to the ULSW and CLSW, defined between 27.68 and 27.74 kg m^{-3}, and 27.74 and 27.82 kg m^{-3}, respectively (Kieke et al., 2006). The integration over time (τ) is shown in orange. The area A on which the subduction rate is calculated is between 52° N to 67° N in latitude and 65° W to 45° W in longitude (cf. black rectangle in Figure 1).

2.4. Subduction Rate Approach

Detrainment (entrainment) is, by definition, the process of a water parcel leaving (entering) the ML temporarily. The instantaneous detrainment rate D is defined as the downward velocity of a parcel of water relative to the base of the ML (Cushman-Roisin, 1987; Nurser & Marshall, 1991):

$$D = -w_b - \frac{Dh}{Dt}, \qquad (1)$$

where $w_b = w_e - \frac{\beta}{f} \int_0^{-h} v dz$, h is the thickness of the ML, w_e is the Ekman pumping velocity, f is the Coriolis parameter, β is the beta plane, and v the horizontal velocity at the base of the ML. This modified Ekman
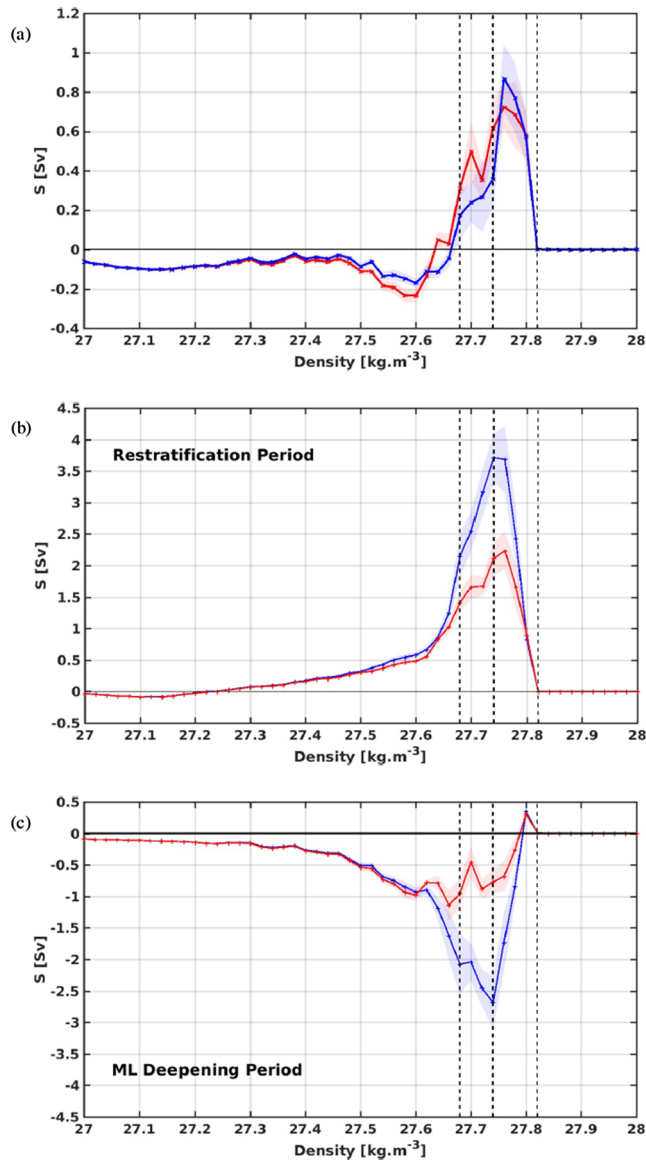
Figure 6. As a function of the potential density (kg m^{-3}), for the 2002–2013 period, we have the mean annual subduction rate S in (a), the seasonal subduction rate S for the restratification period in (b), and the ML deepening period in (c). The units are in Sverdrup (1 Sv = 10^6 m^3 s^{-1}). Calculations using MLD_M are shown in blue, while those using MLD_{TS} are shown in red. The associated shades correspond to the standard error. The vertical dashed lines correspond to the density range of the ULSW and CLSW.

pumping velocity, w_b, takes into account the vertical changes $\left(\frac{dw}{dz}\right)$ at the base of the ML according to the linear vorticity balance (Marshall et al., 1993). The second term on the right-hand side of Equation 1 is the Lagrangian derivative following the horizontal area relative to the base of the instantaneous ML:

$$\frac{D}{Dt} = \frac{\partial}{\partial t} + \mathbf{v} \cdot \nabla. \tag{2}$$

The transfer of fluid leaving (or entering) permanently the ML over a seasonal cycle is called subduction (obduction) (Williams, 2001). While convection occurs in few places in the world, ventilating the deep ocean, subduction is a more ubiquitous process, which ventilates the upper layer of the ocean (Williams, 2001). Figure 5a is a schematic of the subduction/obduction process. During summer (top of Figure 5a), the MLD becomes shallower as the surface layer warms up and the water column becomes more stratified. The parcel of water (shown as a gray square in Figure 5a) virtually crosses the MLD and is thus subducted. In winter (bottom of Figure 5a), the MLD deepens as the convection process occurs and the parcel of water is finally obducted. In order to evaluate the subduction rate S, the detrainment rate D is integrated over a control volume between outcropping isopycnals with density σ and $\sigma + \delta\sigma$ and over a year τ (Da Costa et al., 2005):

$$S(\sigma_h) = \frac{-1}{\tau} \int_0^\tau \int_{A_\sigma} \left[w_b + \frac{\partial h}{\partial t} + \mathbf{v} \cdot \nabla h \right] dA_\sigma dt, \tag{3}$$

where A_σ is the outcrop area defined as $A_\sigma(t) = [x : \sigma \le \sigma_h(x,\, t) \le \sigma + \delta\sigma]$, with σ_h the instantaneous ML density, with $\delta\sigma$ being 0.02 kgm^{-3}. Figure 5b shows a schematic of the ML where each term of Equation 3 is represented. The formal definition of suduction applies to fluid that "escapes" the ML to reach the permanent pycnocline. Under a repeating seasonal cycle, a subducting parcel needs to move laterally or vertically (deeper) to a location where the winter ML depth deepens to a lesser extent in the following winter. Both ULSW and CLSW are defined with a density of 27.68–27.74 kg m^{-3} and 27.74–27.82 kg m^{-3}, respectively. The integration over time discounts all fluid trapped in the seasonal thermocline. The negative sign from Equation 3 defines the subduction process to be positive ($S > 0$) and obduction to be negative ($S < 0$).

3. Subduction Rate

The subduction rate has been calculated for the two different MLDs mentioned above (MLD_M and MLD_{TS}) and is presented in section 3.1. Sections 3.2 and 3.3 show the subduction rates for the upper (27.68–27.74 kg m^{-3}) and classical (27.74– 27.82 kg m^{-3}) LSWs, and for the different components of Equation 3, respectively.

3.1. Impact of MLD Definitions on Subduction Rates

This section shows the impact of the methods used to calculate the MLD over the subduction rate calculation. Figure 6a shows the annual mean subduction rate S in Sverdrup as a function of the potential density from 27 to 28 kg m^{-3}. Up to the density of 27.5 kg m^{-3}, no major difference can be seen between the two methods. Although quantitatively different from 27.52 to 27.82 kg m^{-3}, both results show similar trends. A net obduction of -0.23 Sv $\pm$ 0.03 Sv (red) and -0.17 Sv $\pm$ 0.02 Sv (blue) is evidenced at 27.6 kg m^{-3} for
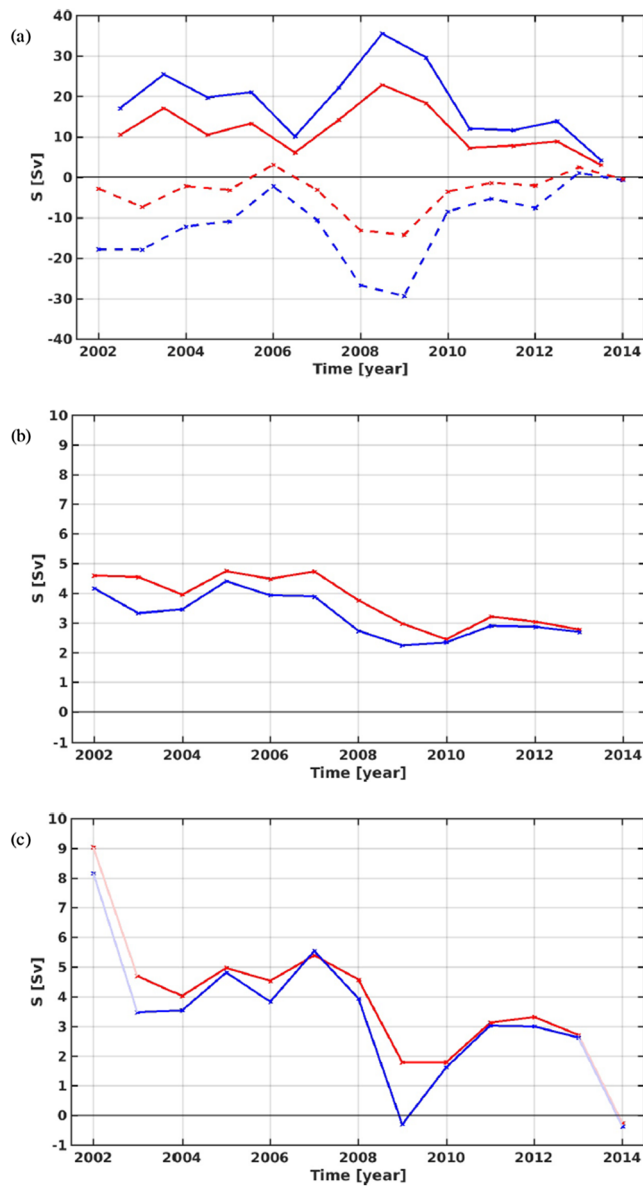
Figure 7. Seasonal net subduction rate S cumulated over the two LSW density classes (27.68–27.82 kg m^{-3}) for the restratification (solid line) and the ML deepening (dash line) periods in (a). Net subduction rate S cumulated over the two density classes (27.68–27.82 kg m^{-3}), from January to December (b) and from July to June (c). Calculations using MLD_M are shown in blue, while those using MLD_{TS} are shown in red. The light color in (c) shows the subduction rates calculated on partial years.

both methods, followed by subduction for the two LSW classes. The fitting-based approach (red) results in two maxima at 27.70 kg m^{-3} (0.50 Sv ± 0.15 Sv) and 27.76 kg m^{-3} (0.72 Sv ± 0.11 Sv), while a maximum of 0.87 Sv ± 0.17 Sv is obtained at 27.76 kg m^{-3} for the MLD_M-based approach (blue).

Another approach is to decompose Figure 6a into two distinct periods: the restratification period from April to September of the same year (Figure 6b) and the ML deepening period from October to March of two consecutive years (Figure 6c). We can see similar trends for both periods. Subduction rates based on MLD_M are approximately double the subduction rates based on MLD_{TS}. For the MLD_M-based approach, up to −2.7 Sv ± 0.4 Sv is obducted during the ML deepening period at 27.74 kg m^{-3}, while 3.7 Sv ± 0.4 Sv is subducted (27.74 kg m^{-3}) during the restratification period. The total net subduction is, then, of 1 Sv ± 0.56 Sv with the density threshold method (MLD_M, in blue). During the ML deepening period of the MLD_{TS} experiment (red), around −0.7 Sv ± 0.24 Sv of LSW reaching 27.76 kg m^{-3} is obducted, while during the restratification period, around 2.2 Sv ± 0.3 Sv is subducted at the same density. A total of 1.5 Sv ± 0.38 Sv net subduction is obtained at the density 27.76 kg m^{-3}, for the fitting method (MLD_{TS}, in red). The conversion from seasonal (cf. Figure 6b or 6c) to annual rate (cf. Figure 6a) is not the sum of the seasonal rates (at 27.76 kg m^{-3}, $S_{ann} = 0.7$ Sv and $S_{seas} = 2.2$–$0.7 = 1.5$ Sv). Indeed, the annual rate is the mean of 12 sums (12 years) of 73 calculations (365 days/5-day input data = 73 output files), while the seasonal rate is the mean (over 12 years) of 12 sums of 31 (or 32) calculations (6 months). This is simply to say that the sum of means is not the mean of the whole data. To approximate the annual rate, we can average the seasonal rates, such as $S_{ann} \sim 0.5 \times (S_{sum} + S_{win})$.

The seasonal net subduction rate S cumulated over the LSW density classes (27.68–27.82 kg m^{-3}) is presented in Figure 7a. As the diagnostic MLD_M is overestimated during deep convection event (Courtois et al., 2017), we can assume that both obduction and subduction are overestimated with S based on MLD_M (seen in blue), compared to S based on MLD_{TS} (red) (c.f. Equation 3). Maximum subduction rate of 35.5 Sv was obtained using the MLD_M method for summer 2008, which is 12.7 Sv larger than S calculated with MLD_{TS} (22.8 Sv). For the ML deepening period, the maximum obduction rates for winter 2009 are −29.4 and −14.3 Sv, for MLD_M and MLD_{TS}, respectively. The rate S with MLD_M is 15.1 Sv larger than S with MLD_{TS}. Figure 7a includes the water mass conversion from one density bin to the next; that is, any density changes in the water mass during the same year will be multiply counted.

The total annual net subduction rate, cumulated over the two density classes (27.68–27.82 kg m^{-3}), is shown in Figure 7b for an average from January to December of the same year, and in Figure 7c from July to June of two consecutive years. Our decision to show both Figures came from our interest in the impact of the time period on which the subduction rate was calculated. In the first case (January to December), winter is divided into two distinct periods, isolating the preconditioning process in the previous year, while keeping the deep convection in the present year. We, thus, considered a year from July to June, keeping the winter season in one part, but not summer. In both cases, the transition between winter and spring, characterizing the restratification period (important feature in the subduction rate), remains in the same year. Straneo (2006), who studied the seasonal variability in the transport of heat and salt through the interior of the LS, indirectly confirmed our choices. Overall, in Figure 7, both rates based on MLD_M and MLD_{TS} show similar pattern. Figure 7b shows an average
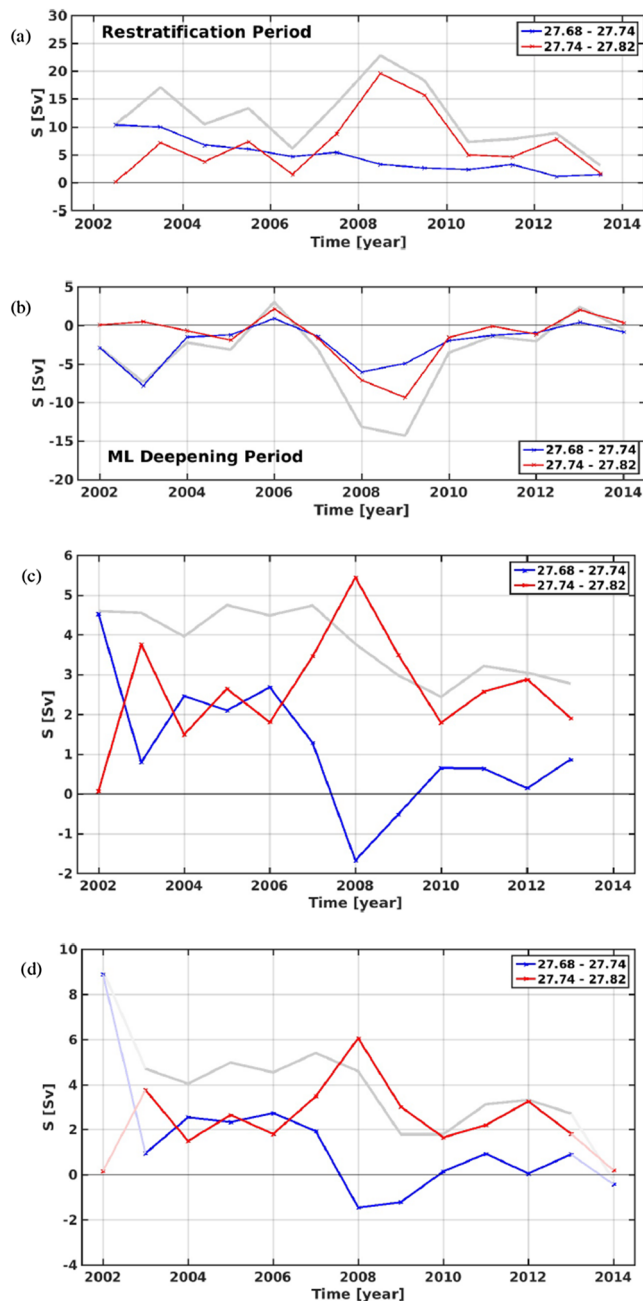
Figure 8. Seasonal net subduction rate S of the ULSW (blue) and CLSW (red) for the restratification (a) and ML deepening (b) periods. The thick gray line represents the total seasonal net subduction for both LSWs. The net subduction rate S of the ULSW (blue) and CLSW (red) from January to December is shown in (c), and from July to June of two consecutive years in (d). The thick gray line represents the total net subduction for both LSWs. The light color in (d) shows the subduction rate calculated over partial years.

subduction rate of 4–4.5 Sv until 2007, followed by a decrease and a plateau around 2.5–3 Sv from 2010. As previously mentioned, Figure 7b has the disadvantage to average the net result by considering two different winters, the one at the beginning of the year and the one at the end of the year. Therefore, the net subduction rate for the 2008 event is partly seen in 2007. Similarly to Figure 7b, the rate S in Figure 7c is around 4 to 5 Sv until 2008, followed by a decrease and a plateau around 3 Sv. The first (2002) and last (2014) data in light color must be carefully considered as the rate is calculated on partial years. A larger variability (−1 to 6 Sv) is visible in Figure 7c. This is more representative, as full winter is considered, without averaging two different winters as it is the case in Figure 7b. Both Figures 7b and 7c do not show a higher rate in 2008, despite the presence of deep convection in the model (Courtois et al., 2017). This is explained by the fact that the obduction and subduction processes cancel out each other as seen in Figure 7a.

Finally, the subduction rates calculated with different MLDs do not differ greatly (see Figure 7), over a seasonal cycle, for the two processes (obduction and subduction) to balance each other. The large difference seen on the subduction rates between the two MLD experiments is evidenced on a short seasonal scale (cf. Figure 6). In the following sections, the subduction rate S is calculated with the MLD_{TS} only (Courtois et al., 2017).

3.2. Subduction Rates of LSWs

Figure 8 shows the net subduction rate for the restratification (a) and ML deepening (b) periods for ULSW (blue) and CLSW (red). A decrease from 10 Sv (2002) to 1 Sv (2013) is clearly shown during the restratification period (a) for ULSW. This trend is also visible during the ML deepening period (b) with two minima in 2003 (−8 Sv) and 2008 (−5 Sv) to finally oscillates around 0 Sv at the end of the simulation. Regarding CLSW, a maximum (minimum) of 20 Sv (−10 Sv) is reached in summer 2008 (winter 2009). This large production of CLSW is in agreement with the 2008 deep convection event mentioned by several studies (Våge et al., 2009; Yashayaev & Loder, 2009). A shift is observed in the LSW density, where the total produced water mass becomes denser. This can be explained by an increase of the salinity field in the model. Figure 9 illustrates the potential density associated with the maximum subduction rate during the restratification period. Although starting at 27.7 kg m^{-3}, which corresponds to the ULSW, the density reaches a plateau between the two water masses (27.74 kg m^{-3}) until 2006, where it increases up to 27.8 kg m^{-3}, corresponding to the CLSW.

Figure 8 also presents the annual net subduction rate S from January to December (c) and from July to June of two consecutive years (d). Both Figures 8c and 8d share similarities, with a subduction rate around 2 Sv up to 2006 for both water masses. From 2007, the ULSW subduction rate, in Figures 8c and 8d, decreases drastically in favor of the CLSW subduction rate, reaching 5.5 Sv (6 Sv) in 2008. After 2010, CLSW has an average subduction rate of 2–3 Sv, while ULSW average subduction rate is around 0.5 Sv. It is worth noting that both Figures 8c and 8d capture the deep convection events of 2003, 2008, and 2012 (Yashayaev & Loder, 2016). The means and standard deviations of the subduction rate of the total LSW (27.68–27.82 kgm^{-3}) are 3.72 Sv ± 1.25 Sv in Figure 8c and 3.78 Sv ± 0.85 Sv in Figure 8d. By comparing only the LSW formation rate, and not the methods used, nor the period considered, these values are in good agreement with previous studies (see Table 1), such as Marsh (2000) (3.9 Sv), Kieke et al. (2006) (3.2–3.3 Sv), or Myers and Donnelly (2008) (2.1–3.9 Sv). However, these values are smaller
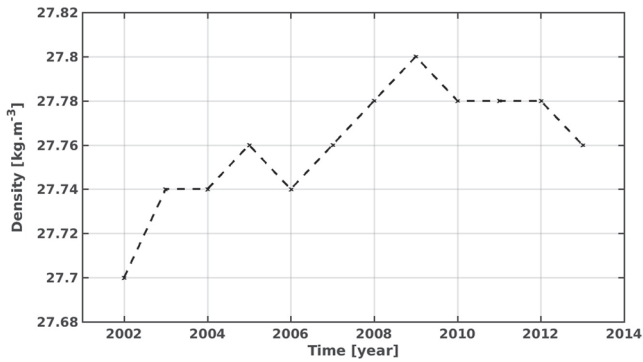
Figure 9. Density obtained for a maximum subduction rate during the restratification period.

than those in Mauritzen and Häkkinen (1999) (8–9 Sv) or Marsh et al. (2005) (7 Sv). Regarding each water mass, the means and standard deviations are 1.16 Sv $\pm$ 1.61 Sv for ULSW and 2.6 Sv $\pm$ 1.36 Sv for CLSW, in Figure 8c, and 0.9 Sv $\pm$ 1.4 Sv for ULSW and 2.8 Sv $\pm$ 1.3 Sv for CLSW, in Figure 8d. The latter results (Figure 8d) were calculated over the full year data, that is, 2002 and 2014 were not taken into account. The low values for ULSW come from its disappearance through the simulation, which can be inferred by the change in the salinity field. The values for the CLSW (2.6–2.8 Sv $\pm$ 1.3 Sv) remains smaller than other studies, such as Smethie and Fine (2001) (7.4 Sv).

The reason why Figures 8c and 8d are similar is that Equation 3 captures the transition between March and April, in both cases. This is a crucial transition, as this period captures the subduction process (see Figure 5a). The absence of CLSW in 2002 is due to the incomplete cooling process as the model starts in January 2002. This implies less mixing and thus shallower MLs, where no CLSW could be produced. The anticorrelation observed between both LSW classes is in agreement with the observations (Kieke et al., 2006), where one water mass is predominant on the other.

3.3. Decomposition of the Subduction Rate

In the present section, the subduction rate for the different components ($w_b, \frac{\partial h}{\partial t}, \nabla uh$, and ∇vh) of Equation 3 is studied and presented. It is relevant to note that we computed $\mathbf{v} \cdot \nabla h$ as $\nabla \mathbf{v} h$, taking advantage of the
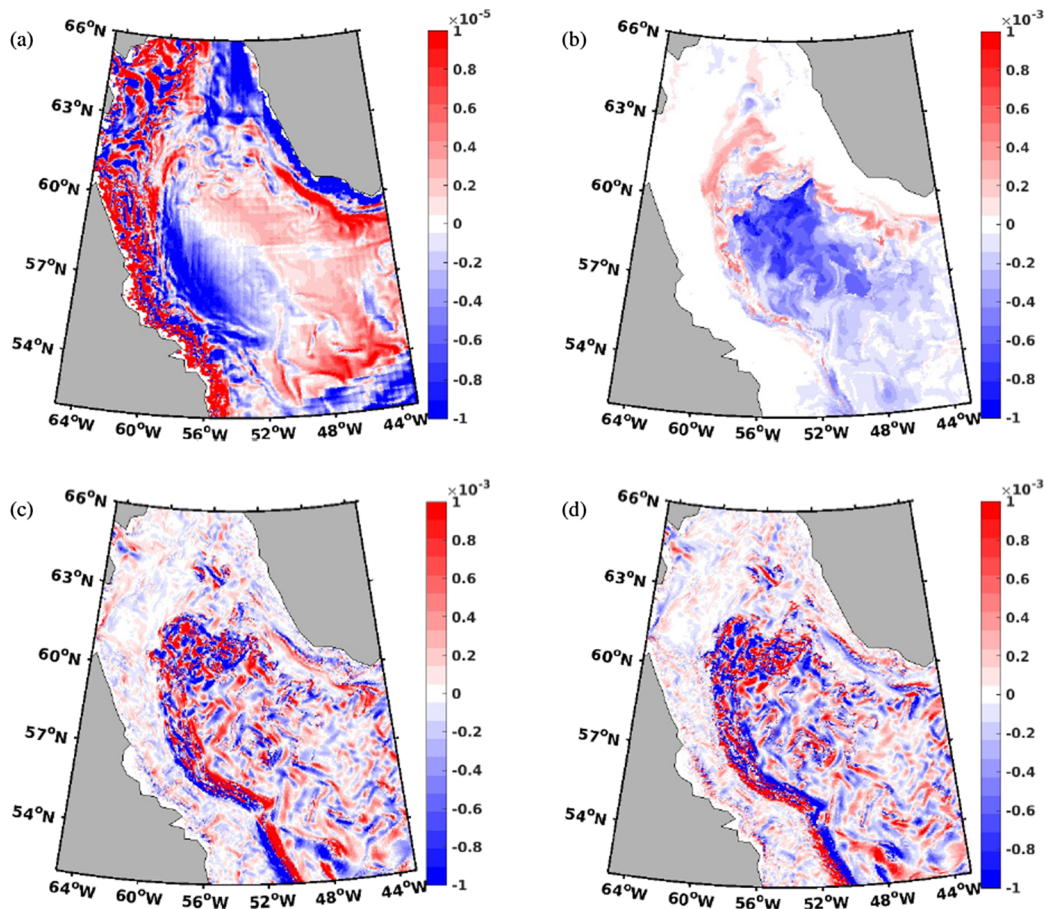

Figure 10. Vertical velocity w_b (a), instantaneous ML $\frac{\partial h}{\partial t}$ (b), zonal advective term (∇uh) (c), and meridional advective term (∇vh) (d), for 5 January 2008 model output. The units are in m s^{-1}. Positive rate S (in red) shows the subduction process (positive downward).
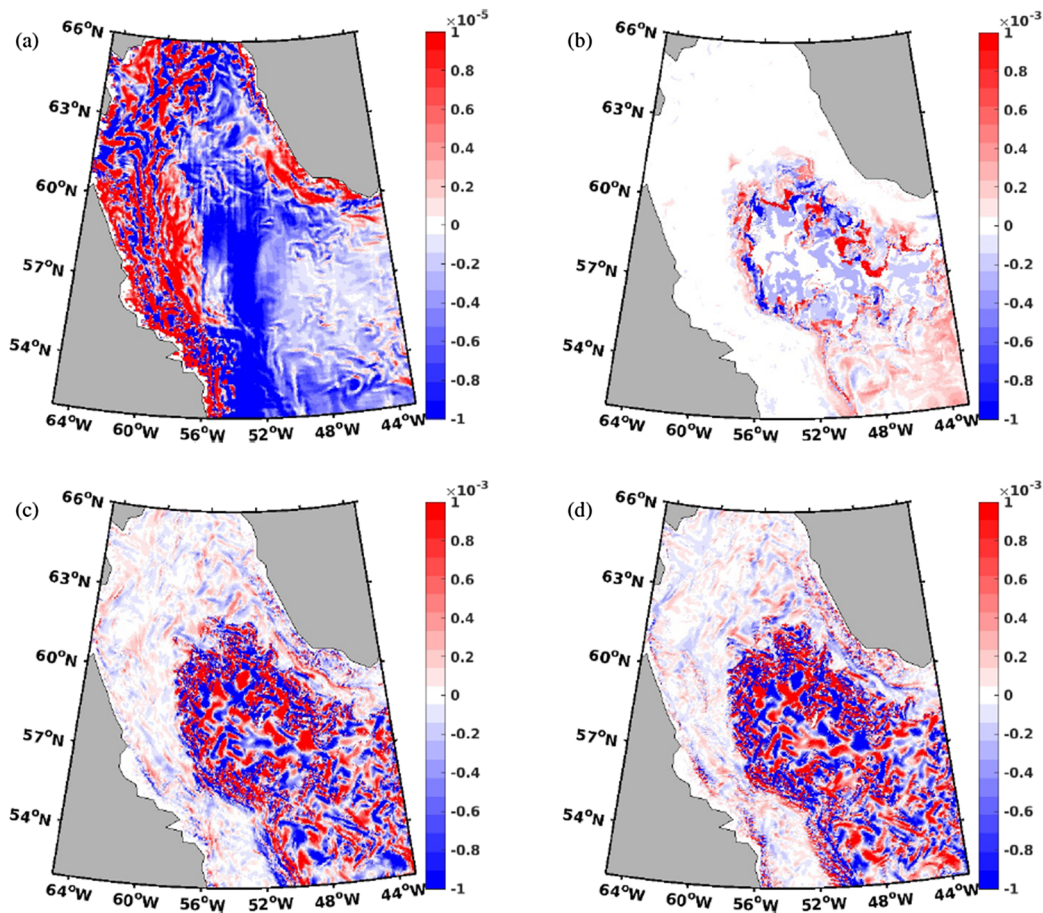
Figure 11. Vertical velocity w_b (a), instantaneous ML $\frac{\partial h}{\partial t}$ (b), zonal advective term (∇uh) (c), and meridional advective term (∇vh) (d), for 16 March 2008 model output. The units are in m s^{-1}. Positive rate S (in red) shows the subduction process (positive downward).

divergence being zero, and thus with ∇uh and ∇vh representing, respectively, the zonal and meridional components of the advection through the sloping base of the ML. Figures 10 and 11 show the four components (m s^{-1}) constituting the subduction rate across winter time of the 2008 model outputs: 5 January and 16 March, respectively. The choice of the model outputs was carefully chosen to show different stages of the subduction process. First, we notice that the vertical component w_b (first line) is 2 orders of magnitude smaller than the other components. In January, we obtain a negative subduction rate (blue) from the instantaneous ML at the center of the LS (Figure 10b), surrounded by positive subduction rate (red) along the boundary currents. Negative subduction rate, that is, obduction process seen in blue, occurs mainly during the winter period (January to March). As the MLD deepens, a fixed water cell will cross the MLD in the upward direction (cf. Figure 5a). In April, the subduction process is predominant (not shown), and from May, the ML displacement tends to stabilise. The horizontal advective terms remain localized along the boundary currents in January when the ML is still shallow (Figures 10c and 10d) but fill the basin in March (Figures 11c and 11d). Similarly to $\frac{\partial h}{\partial t}$, the advective terms almost disappear by May.

The sum of the four components (w_b, $\frac{\partial h}{\partial t}$, ∇uh, and ∇vh) is presented in Figure 12, for 2004 (left) and 2008 (right). We can see a predominance of the advective terms along the boundary currents in January for both years (first line), with deep convection at the center of LS for 2008 (deepening of the MLD; blue area in Figure 12b). In March, the lateral exchange across the ML occurs at the center of LS, but it disappeared along the boundary currents for 2008 (Figure 12d). In April, a few locations of obduction (blue) are still visible in 2004 (Figure 12e), while subduction (red) has now taken place in April 2008 (Figure 12f). By averaging each
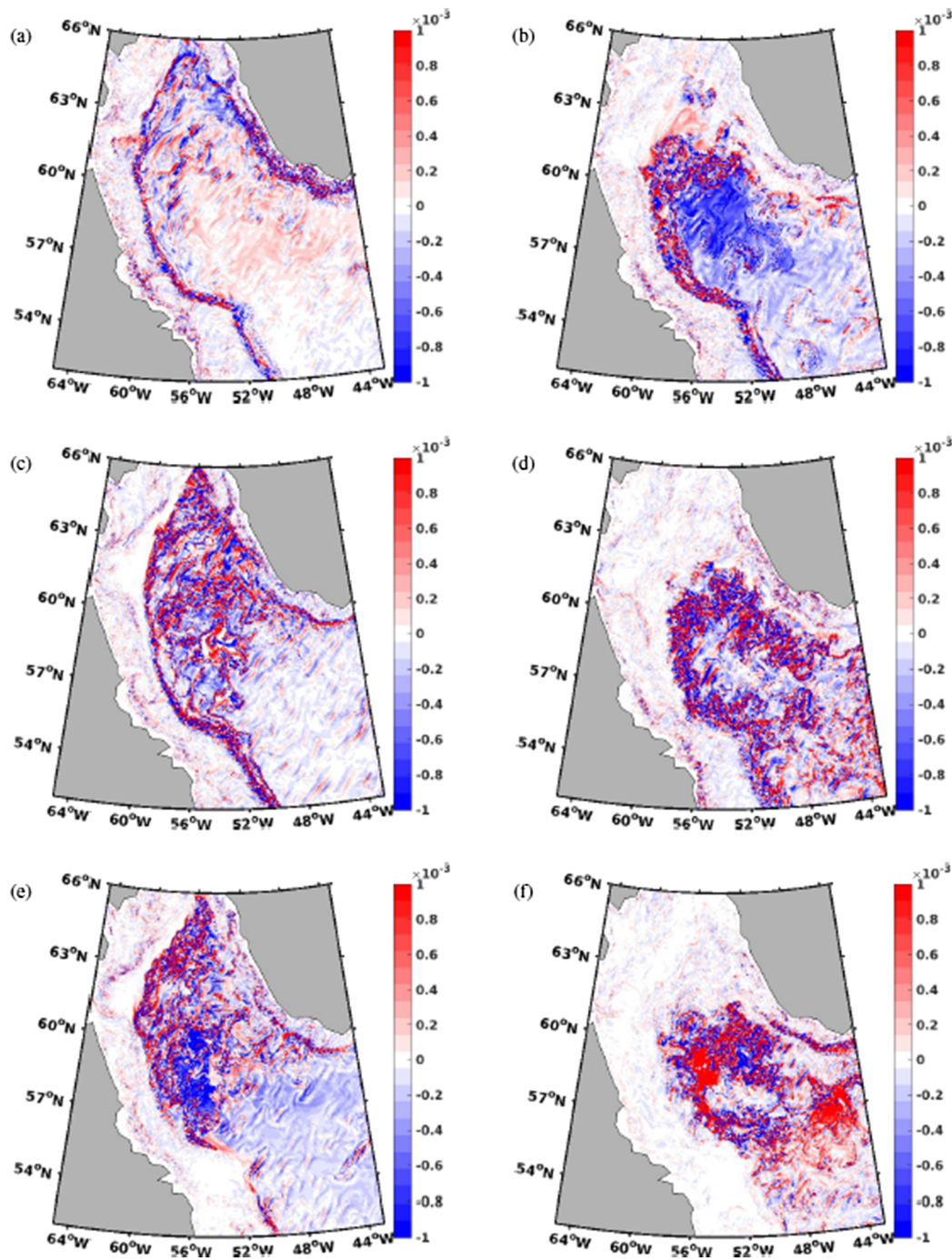
Figure 12. Sum of the four components (w_b, $\frac{\partial h}{\partial t}$, ∇uh, and ∇vh), in m s^{-1}, of the subduction rate, for 2004 (left) and 2008 (right). From top to bottom, the model outputs correspond to 5 January, 16 March, and 15 April. Positive rate S (in red) shows the subduction process (positive downward).

component over the first 3 months of winter (January, February, and March), we can observe predominant features of a component across winter (see Figures 13 and 14). The contribution of the vertical component (Figures 13a and 14a) is emphasized at the continental shelves, where the vertical scale becomes more important compared to the horizontal scales. Although the vertical velocity term is small, it clearly shows the link to vertical flow into and out of the ML associated with the boundary currents and topography. The instantaneous ML change is of a lower order when averaged over 3 months (Figures 13b and 14b). This is expected as the convection process is associated with intermittent MLD changes. This
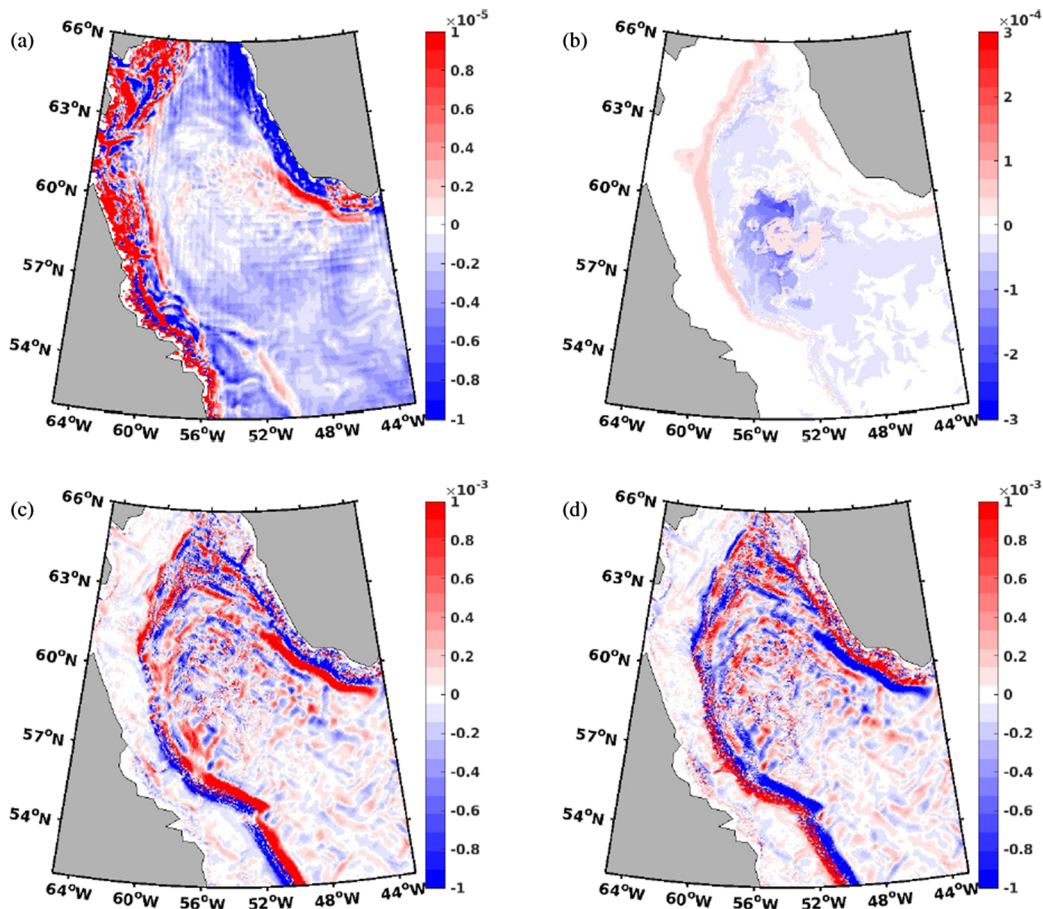
Figure 13. Average of the components (m s^{-1}) of the subduction rate over January, February, and March for 2004. The model outputs correspond to the vertical velocity w_b (a), the instantaneous ML $\frac{\partial h}{\partial t}$ (b), the horizontal advective terms $\nabla u h$ (c), and $\nabla v h$ (d). Positive rate S (in red) shows the subduction process (positive downward).

instantaneous ML change is the most important term on the large scale and thus shows where the MLD is deepening/shallowing, and consequently the obducting/subducting fluid. Areas of deep convection (obduction process) can be observed in blue, in March 2004 (Figure 13b) and March 2008 (Figure 14b), surrounded by subduction process (red) along the boundary currents. The average of the advective terms shows that advection occurs majorly along the boundary currents (Figures 13c, 14c, 13d, and 14d). Although Equation 3 does not provide one with the source of the lateral exchange, we can only speculate that the lateral exchange along the boundary currents could initiate the process of restratification taking place in April. Chanut et al. (2008) show that boundary current eddies convey heat flux from the boundary currents at a sufficient rate to counteract air-sea buoyancy loss, enhancing the restratification throughout the water column.

The previous figures describe every component on a spatial scale. Next, the annual mean subduction rate for the four components as a function of the potential density is quantitatively shown in Figure 15. The obduction rate of the vertical velocity (in black) does not exceed −35 mSv (at 27.70 kg m^{-3}). The rate for the instantaneous ML ($\frac{\partial h}{\partial t}$ in blue) reaches 0.25 Sv at 27.68 kg m^{-3}, increasing up to 0.45 Sv at 27.74 kg m^{-3} and 0.48 Sv at 27.78 kg m^{-3}. The total horizontal advection (in red) depicts a sawtooth-like variation of the subduction rate. With an obduction of −0.085 Sv for the light water mass (at 27.54 kg m^{-3}), the subduction rate shows two major peaks at 27.70 kg m^{-3} with 0.25 Sv and at 27.76–27.80 kg m^{-3} with 0.28 Sv. By decomposing the advective term into zonal and meridional terms, up to 2 Sv (−2 Sv) is subducted (obducted) for $\nabla v h$ ($\nabla u h$) at 27.72 kg m^{-3}. Despite large advective terms ($\nabla v h$ and $\nabla u h$), they balance each other on very small scale.
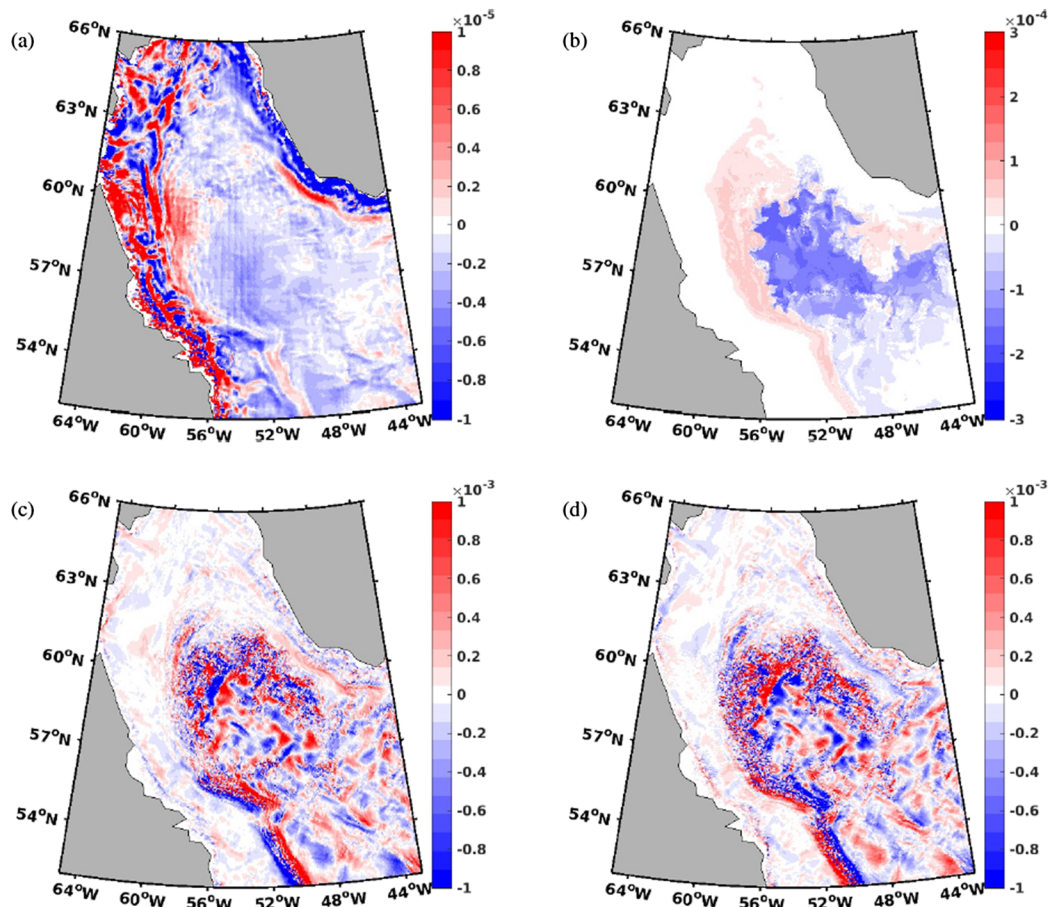
Figure 14. Average of the components (m s^{-1}) of the subduction rate over January, February, and March for 2008. The model outputs correspond to the vertical velocity w_b (a), the instantaneous ML $\frac{\partial h}{\partial t}$ (b), the horizontal advective terms ∇uh (c), and ∇vh (d). Positive rate S (in red) shows the subduction process (positive downward).
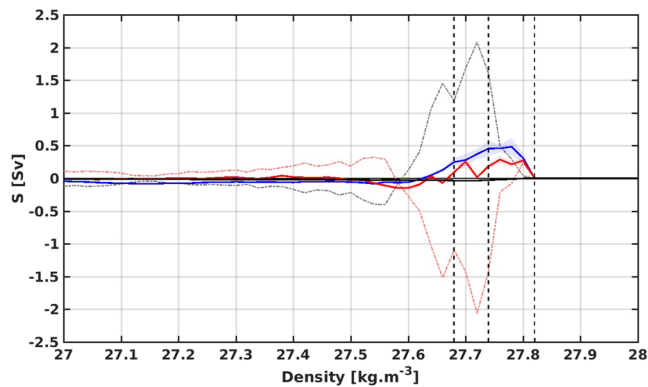

Figure 15. Time averaged components (Sv) as a function of the potential density (kg m^{-3}), for the 2002–2013 period. The vertical velocity w_b is shown in black, the instantaneous ML $\frac{\partial h}{\partial t}$ in blue, and the horizontal advective terms ∇uh and ∇vh in pink and gray, respectively. The sum of the latter terms is in red. For sake of clarity, the standard error is only shown for w_b, $\frac{\partial h}{\partial t}$, and the total advective term, with their associated color. The vertical dashed lines limit the density of the two LSW classes (ULSW and CLSW).

Associated with small-scale MLD variations, the advection is still responsible for almost half of the net subduction at maximum densities.

Figures 16a and 16b show the annual mean of the subduction rate from January to December for the components of Equation 3 over the two LSW classes (27.68–27.82 kg m^{-3}). The rate of the vertical velocity seen in black does not exceed −0.3 Sv on average (−0.32 Sv in 2009). The instantaneous ML term (seen in blue) shows an average subduction rate of 3.1 Sv ± 0.4 Sv up to 2008 and a slight decrease for the rest of the simulation, with a minimum of 1.5 and 1.25 Sv, in 2010 and 2013, respectively. The two advective terms, seen in Figure 16b, show two maxima in 2007 and 2009. Up to −12.2 Sv (in 2007) and −10.1 Sv (in 2009) are obducted for the meridional term ∇uh, while 14.2 Sv (in 2007) and 11.2 Sv (in 2009) are subducted for the zonal term ∇vh. This leads to a maxima of the total water mass advected through the ML of 2 Sv in 2007. The mean of each term over the 12 years of simulation is −161 mSv ± 96 mSv for the vertical component, 2.60 Sv ± 0.76 Sv for the $\frac{\partial h}{\partial t}$ term, and 1.32 Sv ± 0.33 Sv for the advective term (−6.50 Sv ± 3.28 Sv and 7.89 Sv ± 3.4 Sv for the meridional and zonal advective terms, respectively).
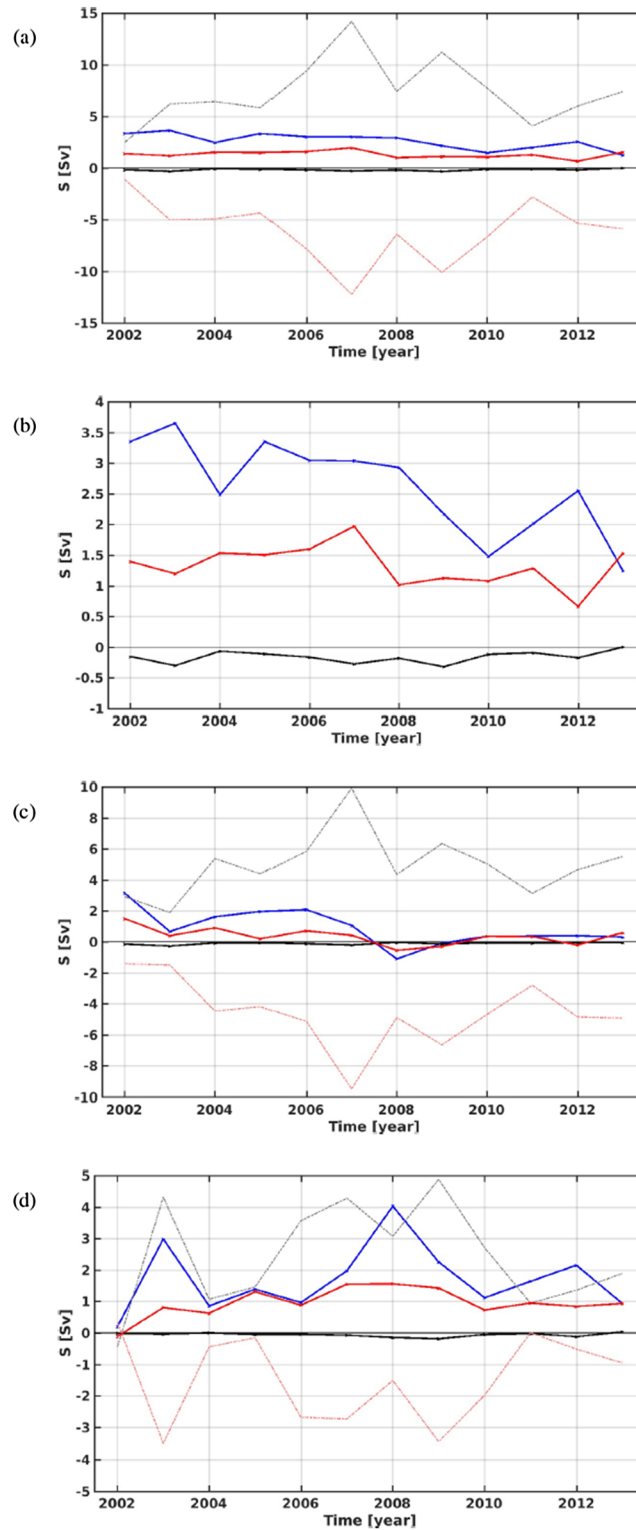
Figure 16. Components of the subduction rate cumulated over the two density classes (27.68–27.82 kg m^{-3}) as a function of time (year), from January to December (a). The vertical velocity w_b is shown in black, the instantaneous ML $\frac{\partial h}{\partial t}$ in blue, and the horizontal advective terms $\nabla u h$ and $\nabla v h$ in pink and gray, respectively. The sum of the latter terms is in red. Panel (b) is panel (a) without the meridional and zonal terms (dashed lines). In (c) and (d), components of the subduction rate for each density class (c: 27.68–27.74 kg m^{-3}; d: 27.74–27.82 kg m^{-3}) as a function of time (year), from January to December.

Figures 16c and 16d are the decomposition of Figures 16a and 16b for the two LSWs, such as the annual mean subduction rates for 27.68–27.74 kg m^{-3}, and 27.74–27.82 kg m^{-3} are seen in Figures 16c and 16d, respectively. The most striking feature of Figure 16 is the decrease of S for the two major components ($\frac{\partial h}{\partial t}$ in blue and the total of the advective terms in red) for the ULSW (Figure 16c), in contrast to the increase of these terms in Figure 16d for the CLSW. The instantaneous ML term for the CLSW reaches a maximum of 4 Sv in 2008, and the total advective term increases up to 1.5 Sv. Once again, the three major deep convection events stated by Yashayaev and Loder (2016) are visible in Figure 16d (2003, 2008, and 2012). The mean of the $\frac{\partial h}{\partial t}$ term is 1.75 Sv $\pm$ 1.2 Sv for the CLSW (cf. Figure 16d), while it is 1.1 Sv $\pm$ 1.3 Sv for the ULSW (Figure 16c). It is worth noting that despite large meridional (-10 Sv in 2007) and zonal (10 Sv in 2007) advective terms for the ULSW, the total term is smaller than 1 Sv (mean: 0.4 Sv $\pm$ 0.6 Sv). In contrast, both advective terms for the CLSW vary between -4 and 5 Sv, but the total shows a net subduction rate of 1 Sv $\pm$ 0.5 Sv. This highligts the stronger advection in the upper layer.

4. Summary and Discussion

As discussed in section 1, the LS is one of the few places where deep convection takes place, allowing gas and heat exchanges between the atmosphere and the deep ocean. This results in LSW, a cold and fresh water mass produced by winter convection. With formation driven by strong winter heat fluxes, and impacted by freshwater input and stratification, highly variable formation rates, for different modes of LSW, have been estimated from many studies. This variability is a function both of the interannual variability impacting the system, but also from many uncertainties and aspect of the different approaches used (briefly summarized in section 1). Given questions about the role of LSW formation in AMOC, with OSNAP having goals of quantifying this linkage, it is important to have quantitative and robust measures to estimate LSW formation rates in a consistent manner, especially for the models that are used to look at the longer timescales and system interlinkage. So we have gone back to the works of Cushman-Roisin (1987), Da Costa et al. (2005), Marshall et al. (1993), and Williams (2001) to examine and quantify LSW formation, using an instantaneous kinematic subduction rate approach. The advantages of this approach is to consider the direct interaction of the ML and the interior of the ocean, by considering vertical and lateral exchanges through the ML base. In this present work, we carry out our analysis of the subduction rate of LSW, using a 1/12° NEMO regional model configuration integrated from 2002 to 2013. We first consider the impact of the MLD definition on the subduction rate. We used two different MLDs, one provided by the suite of model diagnostic output MLD_M and the other calculated from a fitting method over temperature and salinity profiles (MLD_{TS}) (Courtois et al., 2017). Although the MLD plays an important role in the calculation of the subduction rate, especially during the deep convection events, there was no major difference on the annual-mean subduction between these two MLDs. This was explained by the subduction-obduction processes balancing out over an annual timescale. This is an important result related to using this approach to estimate subduction and water formation in numerical models. Given that most models overestimate the ML depth in the LS (as discussed in Courtois et al., 2017), this suggests that the models might still be able to provide more correct water formation rates even when their ML is too deep.

We examined each term of the subduction process (Equation 3): the instantaneous ML term $\left(\frac{\partial h}{\partial t}\right)$, the advective through the sloping base of the ML terms (∇uh, and ∇vh), and the vertical velocity term (w_b). They all impact the subduction rate differently, depending on the time of the year and the location in the LS. The vertical velocity is very small and, with a magnitude less than 0.1 Sv, plays only a very small role in the overall annual subduction process. In fact, this term is associated with net obduction (Figure 15), consistent with broad upwelling over the subpolar gyre interior (Figures 13 and 14). Positive values of subduction associated with the vertical velocity term are generally found around the edge of the basin, linked to the boundary currents and shelf, as well as south of Greenland (Figures , 10,13, and 14). This is consistent with studies that indicate sinking associated with the AMOC is found near the boundary (e.g., Georgiou et al., 2019; Katsman et al., 2018; Netherlands). Yet, given that the vertical velocity term is the smallest in the annual subduction budget, it may be that while the actual sinking is important for the AMOC, it is of less importance compared to vertical mixing and convection for subduction and ventilation.

Obduction related to the deepening of the ML through early winter occurs in the gyre interior in a broad area throughout the interior of the basin (Figure 10b). During this early winter time period, the majority of the subduction that is occurring is in the boundary currents (Figure 12). As deep convection reaches a maximum through March, both the instantaneous ML term and the advective term act on much smaller scales related to local changes in properties. This is consistent with observations that suggest MLD rapidly deepens and shoals on short timescales (Koelling et al., 2017), varying greatly with location (Frajka-Williams et al., 2014; Lilly et al., 1999). As the basin restratifies, strong obduction first occurs at the north and south edges of the convection region prior to obduction in the central convective region in late April and May. The advective terms are very patchy with flow in and out of ML, partially cancelling out, although as a whole, these terms contribute to the next subduction (Figure 15). Maximum subduction in Spring would be consistent with Holte and Straneo (2017), who found the largest overturning in the LS also occurred in Spring, corresponding to the outflow of recently formed LSW. Yashayaev and Loder (2016) also found that the LSW reached its maximum volume at the end of winter (March to April—generally earlier in strong convection winters) before decaying to a minimum early in the following winter.

The subduction rate for both MLDs was around 4–5 Sv up to 2008, followed by a decrease to 3 Sv (cf. Figure 10a). The impact of the MLD was much more visible on a seasonal scale, where each process can be clearly identified. We found that results with MLD_M can be twice as much as those obtained with MLD_{TS}. Thus, it is at this timescale that model issues with ML depths will become apparent in their water mass formation rates. Over the whole simulation (2002–2013), the results showed a decrease of the ULSW production in favor of CLSW. The drift in the salinity field in the model impacts the resulting LSW density. Both water masses have a subduction rate of 2–3 Sv up to 2008 (cf. Figure 14a). Then, 6 Sv of CLSW is subducted in 2008, compared to 1.5 Sv of obducted ULSW. After 2010, both classes are subducted with 2–3 Sv of CLSW and less than 1 Sv of ULSW. The higher CLSW subduction rate found in 2003, 2008, and 2012 coincides with the deep convection events mentioned by Yashayaev and Loder (2016). We note that larger subduction rate during these years of strong deep convection events is associated with peaks in the instantaneous ML depth term. Deeper MLs mean more water to restratify and subduct in these cold winters. Our values regarding the total LSW production are comparable with the values found in the literature (e.g., Pickart & Spall, 2007, with 2 Sv; Myers & Donnelly, 2008, with 2.1–3.9 Sv).

There are still large differences in the literature between different estimates of mean long-term formation of LSW. Circulation- and transformation-based estimates of LSW formation are generally smaller, in the 1.5–3.0 Sv range (e.g., Myers & Donnelly, 2008; Pickart & Spall, 2007). Tracer-based estimates that measure the ventilation of LSW are generally larger, for example, 4.4–5.6 Sv for 1970–1997 (Rhein et al., 2002). Estimates from these different approaches are not incompatible, even for the same year, as they measure different features. Larger values for "seasonal" obduction/subduction are consistent with significant rates associated with tracer ventilation and surface gas exchange. Yet because much of this water is just exchanged across the ML base over the annual cycle, which is the key for tracer ventilation and gas take-up, the actual net subduction rate, which is more important to the circulation and thus the MOC, is much smaller. Accordingly, Lozier et al. (2019) showed a small overturning from their west LS section (from a 21-month observational time series —OSNAP), despite strong convection in the LS. Despite that, our results of significant ventilation through obduction show that the LS is still crucial to the global climate system, in terms of its important role in the uptake of oxygen (Koelling et al., 2017) and anthropogenic carbon (e.g., Rhein et al., 2017).

References

Bamber, J. L., Tedstone, A. J., King, M. D., Howat, I. M., Enderlin, E. M., van den Broeke, M. R., & Noel, B. (2018). Land ice freshwater budget of the Arctic and North Atlantic oceans: 1. Data, methods, and results. *Journal of Geophysical Research: Oceans*, *123*, 1827–1837. https://doi.org/10.1002/2017JC013605

Bamber, J., van den Broeke, M., Ettema, J., Lenaerts, J., & Rignot, E. (2012). Recent large increases in freshwater fluxes from Greenland into the North Atlantic. *Geophysical Research Letters*, *39*, L19501. https://doi.org/10.1029/2012GL052552

Belkin, I. M., Levitus, S., Antonov, J., & Malmberg, S.-A. (1998). "Great Salinity Anomalies" in the North Atlantic. *Progress in Oceanography*, *41*(1), 1–68.

Biló, T. C., & Johns, W. E. (2019). Interior pathways of Labrador Sea Water in the North Atlantic from the Argo perspective. *Geophysical Research Letters*, *46*(6), 3340–3348. https://doi.org/10.1029/2018GL081439

Böning, C. W., Behrens, E., Biastoch, A., Getzlaff, K., & Bamber, J. L. (2016). Emerging impact of greenland meltwater on deepwater formation in the North Atlantic Ocean. *Nature Geoscience*, *9*(7), 523–527 English.

Böning, C. W., Bryan, W., Holland, W. R., & Döscher, R. (1996). Deep-water formation and meridional overturning in a high-resolution model of the North Atlantic. *Journal of Physical Oceanography*, *26*, 1142–1164.

Böning, C. W., Scheinert, M., Dengg, J., Biastoch, A., & Funk, A. (2006). Decadal variability of subpolar gyre transport and its reverberation in the North Atlantic overturning. *Geophysical Research Letters*, *33*, L21S01. https://doi.org/10.1029/2006GL026906

Brandt, P., Funk, A., Czeschel, L., Eden, C., & Böning, C. W. (2007). Ventilation and transformation of Labrador Sea Water and its rapid export in the deep Labrador Current. *Journal of Physical Oceanography*, *37*(4), 946–961. https://doi.org/10.1175/JPO3044.1

Chanut, J., Barnier, B., Large, W., Debreu, L., Penduff, T., Molines, J. M., & Mathiot, P. (2008). Mesoscale eddies in the Labrador Sea and their contribution to convection and restratification. *Journal of Physical Oceanography*, *38*(8), 1617–1643. https://doi.org/10.1175/2008JPO3485.1

Clarke, R. A., & Gascard, J.-C. (1983). The formation of Labrador Sea Water. Part I: Large-scale processes. *Journal of Physical Oceanography*, *13*(10), 1764–1778.

Courtois, P., Hu, X., Pennelly, C., Spence, P., & Myers, P. G. (2017). Mixed layer depth calculation in deep convection regions in ocean numerical models. *Ocean Modelling*, *120*, 60–78.

Cuny, J., Rhines, P. B., Niiler, P. P., & Bacon, S. (2002). Labrador Sea boundary currents and the fate of the Irminger sea water. *Journal of Physical Oceanography*, *32*(2), 627–647. https://doi.org/10.1175/1520-0485(2002)032<0627:LSBCAT>2.0.CO;2

Cushman-Roisin, B. (1987). Subduction. Dynamics of the oceanic surface mixed layer 181–196.

Da Costa, M. V., Mercier, H., & Treguier, A. M. (2005). Effects of the mixed layer time variability on kinematic subduction rate diagnostics. *Journal of Physical Oceanography*, *35*(4), 427–443.

Dai, A., Qian, T., Trenberth, K. E., & Milliman, J. D. (2009). Changes in continental freshwater discharge from 1948 to 2004. *Journal of Climate*, *22*(10), 2773–2792.

Dai, A., & Trenberth, K. E. (2002). Estimates of freshwater discharge from continents: Latitudinal and seasonal variations. *Journal of Hydrometeorology*, *3*(6), 660–687.

de Jong, M. F., Bower, A. S., & Furey, H. H. (2014). Two years of observations of warm-core anticyclones in the Labrador Sea and their seasonal cycle in heat and salt stratification. *Journal of Physical Oceanography*, *44*(2), 427–444. https://doi.org/10.1175/JPO-D-13-070.1

Dickson, R., Lazier, J., Meincke, J., & Rhines, P. (1996). Long-term coordinated changes in the convective activity of the North Atlantic. *Decadal Climate Variability* (pp. 211–261). Berlin: Springer. https://doi.org/10.1007/978-3-662-03291-6_5

Dickson, R. R., Meincke, J., Malmberg, S.-A., & Lee, A. J. (1988). The "great salinity anomaly" in the northern North Atlantic 1968–1982. *Progress in Oceanography*, *20*(2), 103–151.

Ferry, N., Parent, L., Garric, G., Barnier, B., & Jourdain, N. C. (2010). Mercator global Eddy permitting ocean reanalysis GLORYS1V1: Description and results. *Mercator-Ocean Quarterly Newsletter*, *36*, 15–27.

Fichefet, T., & Maqueda, M. (1997). Sensitivity of a global sea ice model to the treatment of ice thermodynamics and dynamics. *Journal of Geophysical Research (1978–2012)*, *102*(C6), 12,609–12,646. https://doi.org/10.1029/97JC00480

Frajka-Williams, E., Rhines, P. B., & Eriksen, C. C. (2014). Horizontal stratification during deep convection in the Labrador Sea. *Journal of Physical Oceanography*, *44*(1), 220–228. https://doi.org/10.1175/JPO-D-13-069.1

Fratantoni, P. S., & Pickart, R. S. (2007). The western North Atlantic shelfbreak current system in summer. *Journal of Physical Oceanography*, *37*(10), 2509–2533.

Gary, S. F., Lozier, M. S., Biastoch, A., & Böning, C. W. (2012). Reconciling tracer and float observations of the export pathways of Labrador Sea Water. *Geophysical Research Letters*, *39*, L24606. https://doi.org/10.1029/2012GL053978

Gascard, J.-C., & Clarke, R. A. (1983). The formation of Labrador Sea Water. Part II. Mesoscale and smaller-scale processes. *Journal of Physical Oceanography*, *13*(10), 1779–1797.

Gelderloos, R., Katsman, C. A., & Drijfhout, S. S. (2011). Assessing the roles of three eddy types in restratifying the Labrador Sea after deep convection. *Journal of Physical Oceanography*, *41*(11), 2102–2119.

Gelderloos, R., Straneo, F., & Katsman, C. A. (2012). Mechanisms behind the temporary shutdown of deep convection in the Labrador Sea: Lessons from the great salinity anomaly years 1968–71. *Journal of Climate*, *25*(19), 6743–6755.

Georgiou, S., van der Boog, C. G., Brüggemann, N., Ypma, S. L., Pietrzak, J. D., & Katsman, C. A. (2019). On the interplay between downwelling, deep convection and mesoscale eddies in the Labrador Sea. *Ocean Modelling*, *135*, 56–70. https://doi.org/10.1016/J.OCEMOD.2019.02.004

Grist, J. P., Josey, S. A., Boehme, L., Meredith, M. P., Laidre, K. L., Heide-Jørgensen, M. P., et al. (2014). Seasonal variability of the warm Atlantic water layer in the vicinity of the greenland shelf break. *Geophysical Research Letters*, *41*(23), 8530–8537. https://doi.org/10.1002/2014GL062051

Grivault, N., Hu, X., & Myers, P. G. (2018). Impact of the surface stress on the volume and freshwater transport through the Canadian Arctic Archipelago from a high-resolution numerical simulation. *Journal of Geophysical Research: Oceans*, *123*, 9038–9060. https://doi.org/10.1029/2018JC013984

Haine, T., Böning, C., Brandt, P., Fischer, J., Funk, A., Kieke, D., et al. (2008). North Atlantic deep water formation in the Labrador Sea, recirculation through the subpolar gyre, and discharge to the subtropics. *Arctic–Subarctic Ocean Fluxes*. Netherlands: Springer. https://doi.org/10.1007/978-1-4020-6774-7_28

Haine, T. W. N., Curry, B., Gerdes, R., Hansen, E., Karcher, M., Lee, C., et al. (2015). Arctic freshwater export: Status, mechanisms, and prospects. *Global and Planetary Change*, *125*, 13–35.

Holte, J., & Straneo, F. (2017). Seasonal overturning of the Labrador Sea as observed by argo floats. *Journal of Physical Oceanography*, *47*(10), 2531–2543. https://doi.org/10.1175/JPO-D-17-0051.1

Holte, J., & Talley, L. (2009). A new algorithm for finding mixed layer depths with applications to argo data and subantarctic mode water formation. *Journal of Atmospheric and Oceanic Technology*, *26*(9), 1920–1939.

Hu, X., Sun, J., Chan, T. O., & Myers, P. G. (2018). Thermodynamic and dynamic ice thickness contributions in the Canadian Arctic Archipelago in nemo-lim2 numerical simulations. *The Cryosphere*, *12*(4), 1233–1247.

Hughes, K. G., Klymak, J. M., Hu, X., & Myers, P. G. (2017). Water mass modification and mixing rates in a 1/12° simulation of the Canadian Arctic Archipelago. *Journal of Geophysical Research: Oceans*, *122*, 803–820. https://doi.org/10.1002/2016JC012235

Hunke, E., & Dukowicz, J. (1997). An elastic-viscous-plastic model for sea ice dynamics. *Journal of Physical Oceanography*, *27*(9), 1849–1867.

Hurrel, J. W. (1995). Decadal trends in the North Atlantic Oscillation: Regional temperatures and precipitation. *Science*, *269*, 676–679.

Katsman, C. A., Drijfhout, S. S., Dijkstra, H. A., & Spall, M. A. (2018). Sinking of dense North Atlantic waters in a global ocean model: Location and controls. *Journal of Geophysical Research: Oceans*, *123*, 3563–3576. https://doi.org/10.1029/2017JC013329

Khatiwala, S., Schlosser, P., & Visbeck, M. (2002). Rates and mechanisms of water mass transformation in the Labrador Sea as inferred from tracer observations*. *Journal of Physical Oceanography*, *32*(2), 666–686. https://doi.org/10.1175/1520-0485(2002)032<0666: RAMOWM>2.0.CO

Kieke, D., Rhein, M., Stramma, L., Smethie, W. M., LeBel, D. A., & Zenk, W. (2006). Changes in the CFC inventories and formation rates of Upper Labrador Sea Water, 1997-2001. *Journal of Physical Oceanography*, *36*(1), 64–86.

Kieke, D., & Yashayaev, I. (2015). Studies of Labrador Sea Water formation and variability in the subpolar North Atlantic in the light of international partnership and collaboration. *Progress in Oceanography*, *132*, 220–232.

Koelling, J., Wallace, D. W. R., Send, U., & Karstensen, J. (2017). Intense oceanic uptake of oxygen during 2014–2015 winter convection in the Labrador Sea. *Geophysical Research Letters*, *44*, 7855–7864. https://doi.org/10.1002/2017GL073933

Lazier, J. R. (1980). Oceanographic conditions at ocean weather ship Bravo, 1964–1974. *Atmosphere-Ocean*, *18*(3), 227–238.

Lazier, J., Hendry, R., Clarke, A., Yashayaev, I., & Rhines, P. (2002). Convection and restratification in the Labrador Sea, 1990–2000. *Deep Sea Research Part I: Oceanographic Research Papers*, *49*(10), 1819–1835.

Lazier, J. R. N., & Wright, D. G. (1993). Annual velocity variations in the Labrador Current. *Journal of Physical Oceanography*, *23*(4), 659–678. https://doi.org/10.1175/1520-0485(1993)023<0659:AVVITL>2.0.CO;2

Li, F., & Lozier, M. S. (2018). On the linkage between Labrador Sea water volume and overturning circulation in the Labrador Sea: A case study on proxies. *Journal of Climate*, *31*(13), 5225–5241. https://doi.org/10.1175/JCLI-D-17-0692.1

Lilly, J. M., Rhines, P. B., Schott, F., Lavender, K., Lazier, J., Send, U., & D'Asaro, E. (2003). Observations of the Labrador Sea eddy field. *Progress in Oceanography*, *59*(1), 75–176.

Lilly, J. M., Rhines, P. B., Visbeck, M., Davis, R., Lazier, J. R. N., Schott, F., & Farmer, D.(1999). Observing deep convection in the Labrador Sea during winter 1994/95. *Journal of Physical Oceanography*, *29*(8), 2065–2098. https://doi.org/10.1175/1520-0485(1999) 029<2065: ODCITL>2.0.CO;2

Lozier, M. S. (2012). Overturning in the North Atlantic. *Annual Review of Marine Science*, *4*, 291–315.

Lozier, M. S., Bacon, S., Bower, A. S., Cunningham, S. A., de Jong, M. F., de Steur, L., et al. (2017). Overturning in the subpolar North Atlantic program: A new international ocean observing system. *Bulletin of the American Meteorological Society*, *98*(4), 737–752. https://doi.org/10.1175/BAMS-D-16-0057.1

Lozier, M. S., Li, F., Bacon, S., Bahr, F., Bower, A. S., Cunningham, S. A., et al. (2019). A sea change in our view of overturning in the subpolar North Atlantic. *Science*, *363*(6426), 516–521.

Madec, G. (2008). NEMO ocean engine. Note du Pôle de modélisation 27.

Marsh, R. (2000). Recent variability of the North Atlantic thermohaline circulation inferred from surface heat and freshwater fluxes. *Journal of climate*, *13*(18), 3239–3260.

Marsh, R., Josey, S., De Nurser, A. J. G., Cuevas, B., & Coward, A. (2005). Water mass transformation in the North Atlantic over 1985–2002 simulated in an eddy-permitting model. *Ocean Science*, *1*(2), 127–144.

Marshall, J. C., Nurser, A. G., & Williams, R. G. (1993). Inferring the subduction rate and period over the North Atlantic. *Journal of Physical Oceanography*, *23*(7), 1315–1329.

Marshall, J., & Schott, F. (1999). Open-ocean convection: Observations, theory, and models. *Reviews of Geophysics*, *37*(1), 1–64.

Mauritzen, C., & Häkkinen, S. (1999). On the relationship between dense water formation and the "Meridional Overturning Cell" in the North Atlantic Ocean. *Deep Sea Research Part I: Oceanographic Research Papers*, *46*(5), 877–894.

McCartney, M., & Talley, L. (1984). Warm-to-cold water conversion in the northern north atlantic ocean, *14*, 922–935.

Moore, G. W. K., Pickart, R. S., Renfrew, I. A., & Våge, K. (2014). What causes the location of the air-sea turbulent heat flux maximum over the Labrador Sea? *Geophysical Research Letters*, *41*, 3628–3635. https://doi.org/10.1002/2014GL059940

Münchow, A., Falkner, K. K., & Melling, H. (2015). Baffin island and West Greenland Current systems in northern baffin bay. *Progress in Oceanography*, *132*, 305–317.

Myers, P. G., & Donnelly, C. (2008). Water mass transformation and formation in the Labrador Sea. *Journal of Climate*, *21*(7), 1622–1638.

Nurser, A. G., & Marshall, J. C. (1991). On the relationship between subduction rates and diabatic forcing of the mixed layer. *Journal of Physical Oceanography*, *21*(12), 1793–1802.

Parker, A., & Ollier, C. D. (2016). There is no real evidence for a diminishing trend of the atlantic Meridional Overturning Circulation. *Journal of Ocean Engineering and Science*, *1*(1), 30–35.

Pennelly, C., Hu, X., & Myers, P. G. (2019). Cross-isobath freshwater exchange within the north atlantic sub-polar gyre. *Journal of Geophysical Research: Oceans*, *124*, 6831–6853. https://doi.org/10.1029/2019JC015144

Pickart, R. S., Smethie, W. M., Lazier, J. R. N., Jones, E. P., & Jenkins, W. J. (1996). Eddies of newly formed upper Labrador Sea Water. *Journal of Geophysical Research*, *101*(C9), 20,711–20,726.

Pickart, R. S., & Spall, M. A. (2007). Impact of Labrador Sea convection on the North Atlantic Meridional Overturning Circulation. *Journal of Physical Oceanography*, *37*(9), 2207–2227.

Pickart, R. S., Spall, M. A., Ribergaard, M. H., Moore, G. W. K., & Milliff, R. F. (2003). Deep convection in the Irminger Sea forced by the greenland tip jet. *Nature*, *424*(6945), 152–156. https://doi.org/10.1038/nature01729

Rattan, S., Myers, P. G., Treguier, A.-M., Theetten, S., Biastoch, A., & Böning, C. (2010). Towards an understanding of Labrador Sea salinity drift in eddy-permitting simulations. *Ocean Modelling*, *35*(1), 77–88.

Rhein, M., Fischer, J., Smethie, W., Smythe-Wright, D., Weiss, R., Mertens, C., et al. (2002). Labrador Sea Water: Pathways, CFC inventory, and formation rates. *Journal of Physical Oceanography*, *32*(2), 648–665.

Rhein, M., Kieke, D., & Steinfeldt, R. (2015). Advection of North Atlantic deep water from the Labrador Sea to the Southern Hemisphere. *Journal of Geophysical Research*, *120*, 2471–2487. https://doi.org/10.1002/2014JC010605

Rhein, M., Steinfeldt, R., Kieke, D., Stendardo, I., & Yashayaev, I. (2017). Ventilation variability of Labrador Sea Water and its impact on oxygen and anthropogenic carbon: A review. *Philosophical Transactions of The Royal Society A Mathematical Physical and Engineering Sciences*, *375*(2102), 20160321–20160337. https://doi.org/10.1098/rsta.2016.0321

Schulze, L. M., Pickart, R. S., & Moore, G. W. K. (2016). Atmospheric forcing during active convection in the Labrador Sea and its impact on mixed-layer depth. *Journal of Geophysical Research: Oceans*, *121*, 6978–6992. https://doi.org/10.1002/2015JC011607

Smethie, W. M., & Fine, R. A. (2001). Rates of North Atlantic Deep Water formation calculated from chlorofluorocarbon inventories. *Deep Sea Research Part I: Oceanographic Research Papers*, *48*(1), 189–215.

Smith, G. C., Roy, F., Mann, P., Dupont, F., Brasnett, B., Lemieux, J.-F., et al. (2014). A new atmospheric dataset for forcing ice-ocean models: Evaluation of reforecasts using the Canadian global deterministic prediction system. *Quarterly Journal of the Royal Meteorological Society*, *140*(680), 881–894.

Speer, K. G., Isemer, H.-J., & Biastoch, A. (1995). Water mass formation from revised COADS data. *Journal of Physical Oceanography*, *25*(10), 2444–2457.

Speer, K., & Tziperman, E. (1992). Rates of water mass formation in the North Atlantic Ocean. *Journal of Physical Oceanography*, *22*(1), 93–104.

Stewart, K. D., & Haine, T. W. N. (2013). Wind-driven Arctic freshwater anomalies. *Geophysical Research Letters*, *40*(23), 6196–6201. https://doi.org/10.1002/2013GL058247

Straneo, F. (2006). Heat and freshwater transport through the central Labrador Sea. *Journal of Physical Oceanography*, *36*(4), 606–628. https://doi.org/10.1175/JPO2875.1

Sverdrup, H. U., Johnson, M. W., & Fleming, R. H. (1942). *The oceans: Their physics, chemistry, and general biology* (Vol. 7). New York: Prentice-Hall.

Talley, L., & McCartney, M. (1982). Distribution and circulation of Labrador Sea Water. *Journal of Physical Oceanography*, *12*(11), 1189–1205.

Våge, K., Pickart, R. S., Thierry, V., Reverdin, G., Lee, C. M., Petrie, B., et al. (2009). Surprising return of deep convection to the subpolar North Atlantic Ocean in winter 2007–2008. *Nature Geoscience*, *2*(1), 67–72.

van Aken, H. M., De Jong, M. F., & Yashayaev, I. (2011). Decadal and multi-decadal variability of Labrador Sea Water in the north-western North Atlantic Ocean derived from tracer distributions: Heat budget, ventilation, and advection. *Deep Sea Research Part I: Oceanographic Research Papers*, *58*(5), 505–523.

Williams, R. (2001). Ocean subduction. *Management*, *25*, 1.

Worthington, L. V. (1976). *On the North Atlantic circulation. The Johns Hopkins Oceanogr. Stud., No. 6*. Baltimore, USA: The Johns Hopkins University Press.

Wright, W. R. (1972). Northern sources of energy for the deep Atlantic. *Deep Sea Research and Oceanographic Abstracts* (Vol. 19, 12, pp. 865–877). UK: Elsevier. http://www.sciencedirect.com/science/article/pii/0011747172900046

Yang, Q., Dixon, T. H., Myers, P. G., Bonin, J., Chambers, D., & van den Broeke, M. R. (2016). Recent increases in Arctic freshwater flux affects Labrador Sea convection and Atlantic overturning circulation. *Nature Communications*, *7*, 10525. https://doi.org/10.1038/ncomms10525

Yashayaev, I. (2007). Hydrographic changes in the Labrador Sea, 1960–2005. *Progress in Oceanography*, *73*(3), 242–276.

Yashayaev, I., & Clarke, A. (2006). Recent warming of the Labrador Sea. *AZMP Bulletin PMZA*, *5*, 12–20.

Yashayaev, I., & Loder, J. W. (2009). Enhanced production of Labrador Sea Water in 2008. *Geophysical Research Letters*, *36*, L01606. https://doi.org/10.1029/2008GL036162

Yashayaev, I., & Loder, J. W. (2016). Recurrent replenishment of Labrador Sea Water and associated decadal-scale variability. *Journal of Geophysical Research: Oceans*, *121*, 8095–8114. https://doi.org/10.1002/2016JC012046

Yashayaev, I., & Loder, J. W. (2017). Further intensification of deep convection in the Labrador Sea in 2016. *Geophysical Research Letters*, *44*, 1429–1438. https://doi.org/10.1002/2016GL071668

Yashayaev, I., van Aken, H. M., Holliday, N. P., & Bersch, M. (2007). Transformation of the Labrador Sea Water in the subpolar North Atlantic. *Geophysical Research Letters*, *34*, L22605. https://doi.org/10.1029/2007GL031812